



Transceive phase mapping using the PLANET method and its application for conductivity mapping in the brain

Soraya Gavazzi¹  | Yulia Shcherbakova²  | Lambertus W. Bartels^{2,3} |
 Lukas J. A. Stalpers⁴ | Jan J. W. Lagendijk¹ | Hans Crezee⁴ |
 Cornelis A. T. van den Berg^{1,2} | Astrid L. H. M. W. van Lier¹

¹Department of Radiotherapy, University Medical Center Utrecht, Utrecht, The Netherlands

²Center for Image Sciences, University Medical Center Utrecht, Utrecht, The Netherlands

³Image Sciences Institute, Imaging Division, University Medical Center Utrecht, Utrecht, The Netherlands

⁴Department of Radiotherapy, Amsterdam UMC, University of Amsterdam, Amsterdam, The Netherlands

Correspondence

Soraya Gavazzi, Department of Radiotherapy, University Medical Center Utrecht, PO Box 85500, 3508 GA Utrecht, The Netherlands.
 Email: s.gavazzi@umcutrecht.nl

Funding information

Supported by the Dutch Cancer Society (KWF), grant UVA 2014-7197.

Purpose: To demonstrate feasibility of transceive phase mapping with the PLANET method and its application for conductivity reconstruction in the brain.

Methods: Accuracy and precision of transceive phase (ϕ^\pm) estimation with PLANET, an ellipse fitting approach to phase-cycled balanced steady state free precession (bSSFP) data, were assessed with simulations and measurements and compared to standard bSSFP. Measurements were conducted on a homogeneous phantom and in the brain of healthy volunteers at 3 tesla. Conductivity maps were reconstructed with Helmholtz-based electrical properties tomography. In measurements, PLANET was also compared to a reference technique for transceive phase mapping, i.e., spin echo.

Results: Accuracy and precision of ϕ^\pm estimated with PLANET depended on the chosen flip angle and TR. PLANET-based ϕ^\pm was less sensitive to perturbations induced by off-resonance effects and partial volume (e.g., white matter + myelin) than bSSFP-based ϕ^\pm . For flip angle = 25° and TR = 4.6 ms, PLANET showed an accuracy comparable to that of reference spin echo but a higher precision than bSSFP and spin echo (factor of 2 and 3, respectively). The acquisition time for PLANET was ~5 min; 2 min faster than spin echo and 8 times slower than bSSFP. However, PLANET simultaneously reconstructed T_1 , T_2 , B_0 maps besides mapping ϕ^\pm . In the phantom, PLANET-based conductivity matched the true value and had the smallest spread of the three methods. In vivo, PLANET-based conductivity was similar to spin echo-based conductivity.

Conclusion: Provided that appropriate sequence parameters are used, PLANET delivers accurate and precise ϕ^\pm maps, which can be used to reconstruct brain tissue conductivity while simultaneously recovering T_1 , T_2 , and B_0 maps.

KEYWORDS

accuracy, conductivity mapping, ellipse fitting, phase-cycled bSSFP, precision, transceive phase mapping

1 | INTRODUCTION

In MRI, the transceive phase represents the RF phase contribution to the phase of the MR signal. In principle, the MR signal phase effectively corresponds to the transceive phase when measuring at $TE = 0$: at this TE, in fact, the MR signal phase is not affected by time-dependent phase terms such as spectral shifts, off-resonance variations, and gradient-induced eddy currents.¹ As the name suggests, the transceive phase originates from RF transmission and reception processes, which involve both transmit and receive chains of a MR system and the imaged sample (e.g., the human body), and is defined as the sum of the phases of the effective transmit and receive magnetic fields (B_1^+ and B_1^- , respectively).^{2,3} Ideally, the RF transmit magnetic field is circularly polarized to obtain maximum power efficiency in creating transverse magnetization. For a standard clinical MR scanner, this is typically realized by a quadrature drive of a 2-channel birdcage body coil. For magnetic fields $>1.5T$, however, eddy currents (leading to RF attenuation) and displacements currents (leading to wave propagation effects) induced in the human body become significant and result in an elliptically polarized net transmit field, the amplitude and phase of which are spatially inhomogeneous.³⁻⁵ Similarly, these currents induced in the body during reception modulate the amplitude and phase of the RF receive field.^{3,6-8} The transceive phase, reflecting the spatial modulations in the phase of both B_1^+ and B_1^- , is therefore characterized by a spatially varying distribution.

The spatial modulation of the transceive phase is primarily induced by the tissue conductivity, as can be derived from Helmholtz equation.⁹⁻¹¹ This relationship has been validated in simulations^{3,12,13} and experimentally with MR electrical properties tomography (EPT).^{10,11,14-20} The transceive phase has been mapped extensively for conductivity reconstruction in different body sites (e.g., in brain,^{14,20-22} breast,^{23,24} liver,²⁵ pelvis²⁶), especially because tissue conductivity maps hold relevant information for RF safety,^{17,18} diagnostics,^{27,28} and therapeutic applications.²⁹⁻³¹

Besides conductivity mapping, transceive phase maps can also be beneficial for correction purposes in phase-based quantitative applications such as QSM and MR thermometry. Peters and Henkelmann³² and Salim et al.³³ showed that, under certain conditions, erroneous temperature measurements can occur in proton resonance frequency shift thermometry when transceive phase offsets caused by temperature-dependent tissue conductivity are not compensated for. Kim et al.³⁴ and Robinson et al.³⁵ demonstrated that more accurate susceptibility maps were obtained when the transceive phase was removed from the phase image used for QSM processing.

Different MR sequences have been proposed for transceive phase measurement, generally spurred by EPT research: dual-echo gradient echo,¹⁹ multi-echo gradient echo,³⁴ UTE,³⁶ and zero-TE (ZTE³⁷), the latter two being more technically

demanding (e.g. requiring high-performance RF hardware to switch between transmit and receive³⁸). However, spin-echo (SE) is a more frequently used sequence for transceive phase mapping.¹⁷ SE is available for all clinical scanners and returns accurate transceive phase estimates without the need to compensate for B_0 -related phase contribution (as in multi-/dual-echo gradient-echo sequence). SE-based techniques generally have longer acquisition times than short-repetition-time gradient echo techniques. An alternative to SE is the balanced steady state free precession (bSSFP) sequence, the signal phase of which approximately reflects the transceive phase over a large spectral range. bSSFP is characterized by relatively high acquisition speed and high SNR, crucial for differentiation-based EPT methods.^{25,39} Nevertheless, its sensitivity to particular off-resonances results in banding artefacts that compromise both the signal magnitude and phase. Methods to compensate these banding artefacts include acquiring phase-cycled bSSFP,⁴⁰⁻⁴³ dynamic bSSFP with frequency shifts coupled with B_0 map acquisition,⁴⁴ and postprocessing methods.⁴⁵

Recently, we have preliminarily shown a brain transceive phase map free from banding artefacts and off-resonance contamination obtained with the PLANET method, a novel ellipse-fitting approach on phase-cycled bSSFP data.^{46,47} Shcherbakova et al.⁴⁸ originally implemented PLANET to reconstruct T_1 , T_2 , off-resonance (Δf_0) maps, and banding-free magnitude image but recognized the potential of the method for EPT. In this study, we demonstrate how transceive phase maps can be retrieved with PLANET and investigate the attainable accuracy and precision in the human brain. To this aim, we performed numerical simulations and MR experiments on a phantom and on healthy volunteers. Moreover, we compared the transceive phase map obtained from PLANET with those acquired using conventional SE and bSSFP techniques and the conductivity maps reconstructed from these transceive phase maps.

2 | THEORY

2.1 | The phase-cycled bSSFP signal

A mathematical expression for bSSFP signal is described in the Appendix. Figure 1A,B shows the magnitude and phase profiles of a standard bSSFP signal (solid lines). The base period, comprised between the null points of the magnitude profile, can be defined as $[(-2 TR)^{-1}, (2 TR)^{-1}]$. Within this period, the region where the phase exhibits a plateau (i.e., $[(-3 TR)^{-1}, (3 TR)^{-1}]$) is called *pass-band* region; the narrow transition band $[\pm(3 TR)^{-1}, \pm(2 TR)^{-1}]$, where both magnitude and phase vary rapidly, is normally known as *stop-band* region. In the stop-band region, the transverse magnetization vanishes, leading to *banding artefacts* in magnitude and phase images.⁴⁹

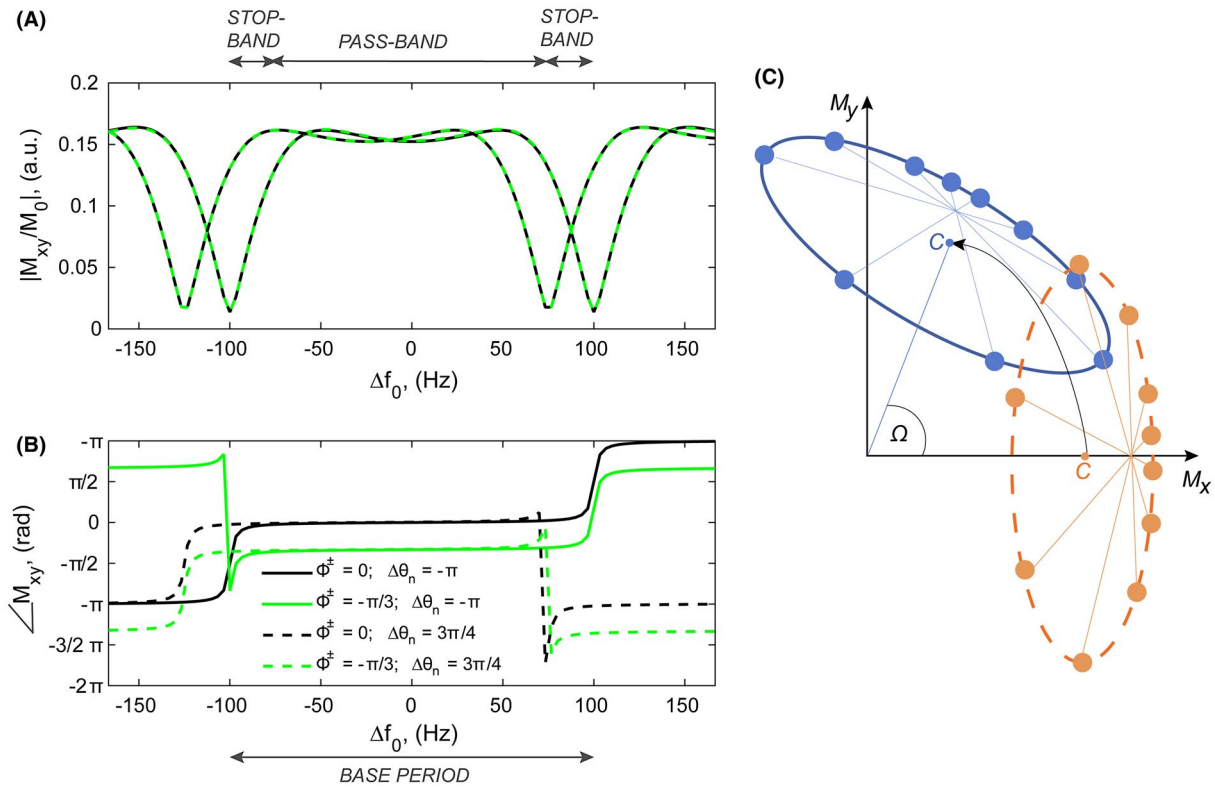


FIGURE 1 Schematic representation of bSSFP and phase-cycled bSSFP signals at the time point equal to TE. A, Magnitude and B, phase of standard bSSFP signal (i.e., bSSFP sequence with a $(0, \pi)$ phase cycling scheme) as a function of off-resonance frequency (Δf_0). The bSSFP signal was simulated for FA = 25°, TR = 5 ms, TE = TR/2, and tissue properties of WM at 3T (WM, $T_1 = 832$ ms, and $T_2 = 80$ ms). Two different values of transceive phase are considered: $\phi^\pm = 0$ rad (black) and $\phi^\pm = -\pi/3$ rad (green). Moreover, two different increments ($\Delta\theta_n$) added to the phase of the RF pulse are shown: $\Delta\theta_n = -\pi$ rad (solid lines) and $\Delta\theta_n = 3\pi/4$ rad (dashed lines). Changing the transceive phase value has no effect on the signal magnitude, but it vertically translates the signal phase of a quantity corresponding to ϕ^\pm . When an increment $\Delta\theta_n \neq -\pi$ is added to the phase of the RF pulse, the magnitude and phase of bSSFP signal shift with frequency. Note that an increment $\Delta\theta_n = -\pi$ rad (solid lines) corresponds to the profile of a standard bSSFP signal. C, Phase-cycled bSSFP signal in the complex plane for a voxel with $\phi^\pm = 0$ rad, $\Delta f_0 \neq 0$ Hz, and increment $\Delta\theta_n = 2n\pi/10 - \pi$ with $n = \{0, 1, 2, \dots, 9\}$. Right after the RF pulse excitation, the phase-cycled data points (coloured dots) lie on the orange ellipse. At TE, the elliptical signal (in blue) is rotated by an angle Ω . The geometrical center of the ellipse is indicated by C. bSSFP, balanced steady state free precession; FA, flip angle; T, Tesla; WM, white matter

Henceforth, we call *standard bSSFP* a bSSFP sequence with standard $(0, \pi)$ RF phase alternation scheme and *phase-cycled bSSFP* a dynamic series of standard bSSFP acquisitions in which each dynamic is acquired with an extra different phase increment $\Delta\theta_n$ added to the standard RF phase cycling scheme. The steady state, phase-cycled signal in a voxel is expressed as⁴³:

$$I_n = KM \cdot e^{-\frac{TE}{T_2}} \cdot \frac{1 - E_2 e^{-i(\theta_0 - \Delta\theta_n)}}{1 - b \cos(\theta_0 - \Delta\theta_n)} \cdot e^{i\Omega}, \quad (1)$$

where $\Delta\theta_n = \frac{2\pi n}{N} - \pi$ with $n = \{0, 1, 2, \dots, N-1\}$ is the user-controlled n^{th} RF phase increment, and N is the total number of RF phase increments. Note that $\Delta\theta_n = -\pi$ returns the standard bSSFP signal described in Appendix Equation A1. Nonetheless, for $\Delta\theta_n \neq -\pi$ both magnitude and phase of the phase-cycled bSSFP signal shift along the off-resonance spectrum (dashed lines in Figure 1A,B). In the complex plane, the phase-cycled

bSSFP data lie on an ellipse for a voxel with only a single component following a Lorentzian frequency distribution (Figure 1C). Right after the RF pulse, this ellipse is rotated around the origin by an angle equal to the transceive phase (ϕ^\pm), whereas it is rotated by an angle Ω (Equation A5) at the TE. For completeness, we mention that the elliptical signal shape might not be maintained if multiple components with different frequency distributions are present in the voxel.⁴⁷

2.2 | Estimation of the transceive phase ϕ^\pm with bSSFP and PLANET

2.2.1 | bSSFP

As shown in Figure 1B, bSSFP signal phase appears almost constant within the pass-band region and shifts vertically by a quantity corresponding to ϕ^\pm value. Thus, the transceive phase is generally approximated by the phase of bSSFP

signal (whereas all other phase contributions in bSSFP phase image $\angle I_0 = \angle(1 - E_2 e^{-i(\theta_0 + \pi)}) \cdot e^{i\Omega}$ [Equation A1] are normally neglected).

2.2.2 | PLANET

PLANET applies a linear least squares fit, specific to ellipses, in the complex plane to steady state phase-cycled bSSFP data using the signal model defined in Equation 1.⁴⁸ This model assumes a Lorentzian single-component relaxation model. To fit the ellipse coefficients in PLANET, at least $N = 6$ dynamics with different RF phase increments are required.⁴⁸ The PLANET method reconstructs T_1 , T_2 , a banding-free image, B_0 -related off-resonances (Δf_0) and ϕ^\pm from the shape and rotation of the ellipse (Figure 1C).

When B_0 drift is assumed negligible and when eddy-current effects are compensated for, the terms ϕ_{drift} and ϕ_{eddy} drop out from the rotation angle Ω in Equation A5, yielding:

$$\Omega = 2\pi \Delta f_0 TE + \phi^\pm. \quad (2)$$

Both Ω and Δf_0 in Equation 2 can be independently estimated from the fitting procedure (see steps 2 and 4 in reference 48). Hence, PLANET-based transceive phase can be obtained by subtracting these two terms.

3 | METHODS

We performed Bloch simulations and MR experiments on a phantom and on healthy volunteers to study the accuracy and precision of the transceive phase retrieved with PLANET method. PLANET performance to map the transceive phase was compared to the performance of a standard bSSFP sequence. Moreover, the experimental transceive phase maps obtained with PLANET, bSSFP and the reference SE were compared and used to reconstruct conductivity maps.

3.1 | Simulations

A phase-cycled bSSFP sequence with standard $(0, \pi)$ RF alternation scheme and $N = 8$ additional RF phase increment steps ($\Delta\theta_n = \frac{2\pi n}{8} - \pi$, with $n = \{0, 1, 2, \dots, 7\}$), as in reference 47, was implemented in MatLab (R2015a, MathWorks, Natick, MA) with a Bloch simulator.⁵⁰ Input parameters for the Bloch simulation comprised sequence parameters (flip angle [FA], TR) and voxel characteristics (Δf_0 , ϕ^\pm , T_1 , and T_2). Rectangular-shaped RF pulses and balanced readout gradients were used. Phase encoding and slice selection gradients were not included. The simulation output was a phase-cycled bSSFP complex signal evaluated at TE after each RF pulse. The signal was considered at steady state after $3 \cdot T_1/\text{TR}$ RF pulses. By applying the PLANET method to this simulated phase-cycled complex signal, the transceive phase for

PLANET was retrieved. The standard bSSFP signal was obtained from phase-cycled bSSFP data at $\Delta\theta_n = -\pi$, the phase of which returned bSSFP-based transceive phase.

Five simulation cases were performed to study the performance of bSSFP and PLANET in estimating ϕ^\pm (see Table 1). Four Monte Carlo simulations (simulations I→IV) evaluated the accuracy and precision of transceive phase values obtained with bSSFP and PLANET as a function of sequence settings (FA and TR in simulations I and III; N in simulation IV), tissue relaxation properties (T_1 and T_2 in simulation IV), and other parameters (Δf_0 and ϕ^\pm in simulation II). In simulations I, II and III, the relaxation times representing white matter (WM) at 3T were used ($T_1 = 832$ ms and $T_2 = 80$ ms.⁵¹). In simulations I, II and IV the transceive phase and off-resonance frequency (fixed parameters) (Table 1) were selected based on the representative experimental values found at 3T in WM in a central portion of the FOV. Simulations I and III differed in the relaxation model used: in simulation I, only the single (Lorentzian) frequency distribution of WM was present in the voxel, whereas simulation III included also a second, smaller component—myelin water—and gives an example of a commonly used, more complex model of human WM tissue^{47,52-55} (details in Table 1, assumed field strength: 3T). For all four cases, Gaussian noise was added independently to both real and imaginary parts of the simulated phase-cycled signal (noise SD $\zeta = 10$, with $M_0 = 10000$), prior to PLANET postprocessing, and the total number of Monte Carlo iterations (Z) was 10,000.

Because PLANET method relies on data in the steady state regime,⁴⁸ the effect of RF dummy pulses on the transceive phase was investigated in simulation V, where a noiseless phase-cycled bSSFP signal was simulated for a voxel containing cerebrospinal fluid (CSF) at 3T. Because of its long T_1 and T_2 , CSF demands the highest number of dummy pulses to reach steady state.

3.2 | Measurements

Phantom and in vivo MR experiments were performed on a 3T clinical scanner (Ingenia, Philips, Best, The Netherlands) with the body coil for transmission and a 15-channel head coil for reception. The vendor-specific Constant Level of Appearance (CLEAR) option was enabled to obtain transceive phase maps free from the complex receive sensitivity of the head coil; this emulates the situation in which the body coil was used in quadrature mode for both transmission and reception.⁵⁶ For both phantom and in vivo measurements, we used a 3D phase-cycled bSSFP sequence with the following parameters: FOV = $240 \times 240 \times 60$ mm³, voxel size = $2.5 \times 2.5 \times 2.5$ mm³, 8 phase increments ($\Delta\theta_n = \frac{2\pi n}{8} - \pi$, with $n = \{0, 1, 2, \dots, 7\}$), FA = 25°, TE = 2.3 ms, TR = 4.6 ms. To minimize transient effects, a series of 2170 dummy pulses was applied before each phase-cycled bSSFP acquisition;

TABLE 1 Overview of simulation cases performed

Name of Simulation	Type of Simulation	Fixed Parameters	Variable Parameters	Figure ^a	Purpose
Simulation I	Monte Carlo	$T_1 = 832$ ms $T_2 = 80$ ms $\phi^\pm = -\pi/3$ rad $N = 8$	$\Delta f_0 = [0; 15; 30]$ Hz FA = $[0 \rightarrow 90]^\circ$ TR = $[3 \rightarrow 33]$ ms	2, 3, S1, S2	Evaluate e_{ϕ^\pm} and ζ_{ϕ^\pm} as a function of FA and TR for a single component voxel in on-resonance and off-resonance conditions
Simulation II	Monte Carlo	$T_1 = 832$ ms $T_2 = 80$ ms FA = 25° TR = 4.6 ms $N = 8$	$\Delta f_0 = [-100 \rightarrow 100]$ Hz $\phi^\pm = [-\pi/2 \rightarrow \pi/2]$ rad	2	Evaluate e_{ϕ^\pm} and ζ_{ϕ^\pm} as a function of Δf_0 and ϕ^\pm for a single component voxel
Simulation III	Monte Carlo	$N = 8$ 1 st component $T_{1,1} = 832$ ms $T_{2,1} = 80$ ms $\phi^\pm_1 = -\pi/3$ rad $w_l = 0.88$ 2 nd component $T_{1,2} = 400$ ms $T_{2,2} = 20$ ms $\phi^\pm_2 = -\pi/3$ rad CS = 20 Hz $w_2 = 0.12 = (1 - w_l)$	$\Delta f_{0,1} = [0; 15]$ Hz $\Delta f_{0,2} = [20; 35]$ Hz FA = $[0 \rightarrow 90]^\circ$ TR = $[3 \rightarrow 33]$ ms ($\Delta f_{0,2} = \Delta f_{0,1} + \text{CS}$)	2, 3, S1, S2	Evaluate e_{ϕ^\pm} and ζ_{ϕ^\pm} as a function of FA and TR for a 2-component voxel in on-resonance and off-resonance conditions. The 2 components considered were WM (1 st component, with WM fraction w_l) and myelin (2 nd component, with myelin fraction w_2)
Simulation IV	Monte Carlo	$\Delta f_0 = 0$ Hz $\phi^\pm = -\pi/3$ rad FA = 25° TR = 4.6 ms	$T_1 = [100 \rightarrow 4000]$ ms $T_2 = [20 \rightarrow 500]$ ms $N = [6 \rightarrow 10]$	4	Calculate C_{ϕ^\pm} as a function of T_1 and T_2 and as a function of N
Simulation V	Simple (noise-free, 1 iteration)	$T_1 = 3858$ ms $T_2 = 500$ ms $\Delta f_0 = 15$ Hz $\phi^\pm = -\pi/3$ rad FA = 25° TR = 4.6 ms $N = 8$	#RF = $[500 \rightarrow 2500]$ #RF: number of RF dummy pulses	S3	Evaluate e_{ϕ^\pm} as a function of #RF

Note: All parameters values are at 3T.

FA = flip angle; T = tesla; S, supporting information figure; WM = white matter.

^aSupporting Information Figures S1 and S2 present results for simulation I for the cases of $\Delta f_0 = 0$ Hz and $\Delta f_0 = 30$ Hz, as well as the results for simulation III for the case of $\Delta f_{0,1} = 0$ Hz (and $\Delta f_{0,2} = 20$ Hz).

thus, the scan time increased from 2:46 min to 5:20 min. We employed a 2D multi-slice SE sequence as a reference method for transceive phase mapping because it is generally recognized to provide accurate ϕ^\pm values.^{16,17} With the same FOV and voxel size, SE settings were: TE/TR = 5.2/1100 ms (scan time: 7:16 min). Both phase-cycled bSSFP and SE acquisitions were repeated with opposed readout gradient polarities to allow compensation of eddy current effects (see Postprocessing). A reference Δf_0 map was acquired in each

session with 3D dual-echo spoiled gradient-echo sequence (FA = 60° , TE₁/TE₂/TR = 2.3/4.6/30 ms).

Phantom experiments involved a cylindrical phantom (diameter and length: 12 cm) filled with water, 5.1 g/L NaCl, and agar (2% w/v). The resulting homogeneous composition had a conductivity value within the physiologic range for the whole brain,⁵⁷ $\sigma = 0.85$ S/m, which was measured with a dielectric probe (85070E, Agilent Technologies, Santa Clara, CA).

Two independent phantom experiments were conducted by changing the B_0 shimming options to prove the robustness of PLANET-based transceive phase estimation against off-resonance effects. In the first experiment (experiment I), a volumetric B_0 shimming within the FOV was guaranteed; in the second experiment (experiment II), a first-order field variation was enforced by activating the y -shimming gradient (with intensity of 0.3 mT/m). A third experiment (experiment III) investigated the effect of different RF phase increment steps ($N = 6, 8, 10$) on the transceive phase and conductivity.

In vivo brain measurements were approved by the local institutional review board. Images were obtained from 3 healthy volunteers whose written informed consent was obtained beforehand.

3.3 | Postprocessing

Several postprocessing steps were performed in MatLab on the acquired phase-cycled bSSFP and SE signals to obtain transceive phase and conductivity maps. First, a method based on local subvoxel shifts was employed to correct each signal for Gibbs ringing.⁵⁸ Then, the phase images from the two signals acquired with opposed readout gradient polarity were averaged to minimize the phase contribution due to eddy currents (ϕ_{eddy}) (see Equation A5). At this point, SE- and bSSFP-based transceive phase maps were obtained. To retrieve PLANET-based transceive phase map, the PLANET method was applied to both phase-cycled bSSFP acquisitions, and the resulting transceive phase maps were then averaged. If phase wraps appeared, the transceive phase maps were unwrapped by adding a 2π -offset to phase wraps with an in-house region-growing algorithm. Finally, the transceive phase mean value, calculated in the central slice, was subtracted from the transceive phase map for each method to exclude potential global phase constant offsets deriving arbitrarily from the scanner's data acquisition chain. Subtracting the mean value will not influence the conductivity reconstruction, the latter being a derivative-based method that neglects any global offset. For brain data, all phase-cycled images were rigidly registered to SE images after Gibbs ringing correction to reduce the impact of potential interscan head motion during the scan session.

Conductivity maps were reconstructed based on these experimental transceive phase maps. For conductivity reconstruction, a conventional Helmholtz-based, *phase-only* EPT method was applied (Laplacian operator: noise-robust kernel of $7 \times 7 \times 3$ voxels^{19,59}), and the transceive phase assumption was used.^{15,16,18,19}

3.4 | Accuracy

We define *accuracy* as the error between the estimate of the transceive phase and the true (or reference) transceive phase.

For all Monte Carlo simulations (simulations I→IV), the accuracy was calculated as the difference (e_{ϕ^\pm}) between bSSFP- or PLANET-based transceive phase estimate averaged over all Z iterations ($\bar{\phi}^\pm = \frac{1}{Z} \sum_{i=1}^Z \phi_i^\pm$) and the true value ϕ_{true}^\pm (e_{ϕ^\pm} effectively corresponds to a systematic error⁶⁰):

$$e_{\phi^\pm} = |\bar{\phi}^\pm - \phi_{\text{true}}^\pm|. \quad (3)$$

In measurements, knowledge on the true value is lacking. Thus, the accuracy was assessed by the difference $\Delta\phi^\pm$ between bSSFP- or PLANET-based transceive phase and the transceive phase acquired with SE, which is commonly recognized as a reference sequence for transceive phase mapping.¹⁶

3.5 | Precision

We define *precision* as the inverse of the uncertainty of the estimated transceive phase. The uncertainty of the transceive phase is represented by its SD. We denote the uncertainty (or SD) of the transceive phase with ζ_{ϕ^\pm} to avoid confusion with the conductivity symbol σ .

In simulations I→IV, the uncertainty ζ_{ϕ^\pm} was calculated as the SD of the transceive phase estimated with bSSFP or PLANET over all Z iterations (ζ_{ϕ^\pm} corresponds to a random error):

$$\zeta_{\phi^\pm} = \sqrt{\frac{\sum_{i=1}^Z (\phi_i^\pm - \bar{\phi}^\pm)^2}{Z}}. \quad (4)$$

Typically, in experiments the uncertainty of a phase image Φ is approximated with $\zeta_\Phi \cong SNR_{\text{magnitude}}^{-1}$. Such approximation holds for phase images that are directly acquired with any sequence and for noise levels significantly smaller than the signal magnitude.⁶¹ Hence, it could be applicable for bSSFP-based transceive phase but not for PLANET because of the fitting procedure on the acquired signals used to retrieve ϕ^\pm . Assessing analytically the noise propagation related to PLANET fitting is difficult; thus, we followed an empirical approach that ultimately leads to determining the experimental ζ_{ϕ^\pm} . For this purpose, we performed Monte Carlo simulation IV (Table 1), where we related the “true” transceive phase uncertainty calculated with Equation 4, which can only be assessed in simulation, to the “theoretical uncertainty $\tilde{\zeta}_{\phi^\pm}$,” which was based on the aforementioned approximation by Gudbjartsson and Patz⁶¹ and can be assessed in both simulations and measurements. The theoretical uncertainty was defined as:

$$\tilde{\zeta}_{\phi^\pm} = \left(\sqrt{2} \cdot SNR_{\text{magnitude}} \right)^{-1}, \quad (5)$$

where $\sqrt{2}$ accounts for the averaging operation performed to retrieve an eddy-current-free transceive phase map

(see Postprocessing section). The $SNR_{\text{magnitude}}$ was calculated according to the definition of Björk et al.⁴¹:

$$SNR_{\text{magnitude}} = \frac{\sum_{n=0}^{N-1} |I_n(\Delta\theta_n)|}{N \cdot \zeta}, \quad (6)$$

where $|I_n(\Delta\theta_n)|$ is the magnitude of the n^{th} phase-cycled bSSFP signal, ζ is the SD of the Gaussian noise level ($\zeta = 10$) and N is the number of phase-cycled bSSFP acquisitions ($N = 8$).

The simulated true and theoretical uncertainties were compared by computing their ratio $C_{\phi^{\pm}} = \frac{\zeta_{\phi^{\pm}}}{\tilde{\zeta}_{\phi^{\pm}}}$. $C_{\phi^{\pm}}$ accounts for the increase/reduction in the transceive phase noise level occurring during postprocessing (e.g., PLANET fitting) since the noise propagation attributed to the acquisition is already considered in $\tilde{\zeta}_{\phi^{\pm}}$ (for which case, $C_{\phi^{\pm}} = 1$). For minimum uncertainty, $C_{\phi^{\pm}} \rightarrow 0$.

Based on the values for $C_{\phi^{\pm}}$ found in this simulation, we assessed the uncertainty $\zeta_{\phi^{\pm}}$ in experiments with Equation 7:

$$\zeta_{\phi^{\pm}} = C_{\phi^{\pm}} \cdot \tilde{\zeta}_{\phi^{\pm}} = C_{\phi^{\pm}} \cdot \left(\sqrt{2} \cdot SNR_{\text{magnitude}} \right)^{-1}. \quad (7)$$

The experimental $SNR_{\text{magnitude}}$ in Equation 7 was calculated by averaging the SNR maps relative to all phase-cycled images, which conceptually corresponds to Equation 6. These SNR maps were obtained with Kellman and McVeigh's method.⁶²

4 | RESULTS

4.1 | Simulation results

4.1.1 | Simulations I and II

The accuracy of the transceive phase, identified by the error $e_{\phi^{\pm}}$, estimated with bSSFP and PLANET in a voxel containing WM tissue, is illustrated in Figure 2 and in Supporting Information Figure S1. In bSSFP, the error $e_{\phi^{\pm}}$ was 0 on-resonance ($\Delta f_0 = 0$ Hz) (Supporting Information Figure S1) and was independent from FA. Nevertheless, it varied depending on the combination of Δf_0 and TR: for example, $e_{\phi^{\pm}} \approx 0.11$ rad (i.e., $\sim 10.5\%$ of $\phi_{\text{true}}^{\pm} = -\pi/3$ rad) was obtained at TR = 17 ms ($\frac{1}{4\Delta f_0}$, thus within the pass-band region) (Figure 2) for $\Delta f_0 = 15$ Hz and at TR = 11 ms ($\frac{1}{3\Delta f_0}$, i.e., the cutoff for stop-band) (Supporting Information Figure S1) for $\Delta f_0 = 30$ Hz. In general, the error rapidly increased following a sigmoidal curve for TRs $> \frac{1}{4\Delta f_0}$. Differently, in PLANET the error was 0 for any TR $< \frac{1}{2\Delta f_0}$ and any FA $> FA_{\text{Ernst}}$, where $FA_{\text{Ernst}} = \arccos(\exp(-TR/T_1))$ is the minimum FA for which the ellipse does not collapse,⁴⁰ thus hindering PLANET fitting approach (Figure 2 and Supporting Information Figure S1). For TRs $\approx \frac{1}{2\Delta f_0}$, the error exceeded

0.50 rad for FA $> 50^\circ$ (e.g., at TR ≈ 17 ms for $\Delta f_0 = 30$ Hz) (Supporting Information Figure S1). For the fixed parameters used in MR experiments (i.e., FA = 25° and TR = 4.6 ms, simulation II), the following errors were obtained: $e_{\phi^{\pm}} \leq 0.03$ rad for $\Delta f_0 < \frac{1}{4TR} = 50$ Hz and $e_{\phi^{\pm}} > 0.05$ rad for $\Delta f_0 > \frac{1}{3TR} \approx 73$ Hz for bSSFP, whereas no error was observed for any Δf_0 in PLANET.

The uncertainty of the transceive phase ($\zeta_{\phi^{\pm}}$) estimated with bSSFP and PLANET is shown in Figure 3 and Supporting Information Figure S2. Because of their inverse relationship, $\zeta_{\phi^{\pm}}$ and SNR shared similar patterns for both methods. The uncertainty $\zeta_{\phi^{\pm}}$ in bSSFP presented a TR-invariant distribution at $\Delta f_0 = 0$ Hz, with lowest values for FA = $[25-45]^\circ$. A pronounced TR-dependence was observed for increasing values of Δf_0 , which reflected the transition of the signal magnitude from pass-band to stop-band region. Approaching TR $\approx \frac{1}{2\Delta f_0}$ reduced the range of FAs generating lowest $\zeta_{\phi^{\pm}}$ values (Figure 3 and Supporting Information Figure S2). In PLANET, an almost TR-invariant $\zeta_{\phi^{\pm}}$ was observed for any Δf_0 , and the highest precision (i.e., lowest $\zeta_{\phi^{\pm}}$) was found for FA = $[18-30]^\circ$. In this FA range, the uncertainty $\zeta_{\phi^{\pm}}$ in PLANET was approximately half the uncertainty in bSSFP.

4.1.2 | Simulation III

The accuracy and precision of transceive phase estimation can change when a voxel contains multiple components with different relaxation times and frequency distributions. Results are presented for a voxel including WM as the dominant component and myelin water as the second component, in an often used ratio to model human WM tissue.^{47,52-55} With respect to the case of single WM component, the uncertainty patterns were mildly affected (Figure 3 and Supporting Information Figure S2), but the error distribution varied (Figure 2 and Supporting Information Figure S1). For this specific example case, $e_{\phi^{\pm}}$ increased for longer TRs in both bSSFP and PLANET and slightly increased for smaller FAs in bSSFP. For FA = 25° and TR = 4.6 ms (used in experiments), bSSFP was more sensitive than PLANET to myelin presence when $\Delta f_{0,1} = 15$ Hz ($e_{\phi^{\pm}} = 1.4 \cdot 10^{-2}$ rad vs. $e_{\phi^{\pm}} = 5.8 \cdot 10^{-3}$ rad) (Figure 2), but was less sensitive when $\Delta f_{0,1} = 0$ Hz ($e_{\phi^{\pm}} = 3.8 \cdot 10^{-3}$ rad vs. $e_{\phi^{\pm}} = 5.5 \cdot 10^{-3}$ rad) (Supporting Information Figure S1).

4.1.3 | Simulation IV

Figure 4 depicts the constant $C_{\phi^{\pm}}$, used in Equation 7 to estimate $\zeta_{\phi^{\pm}}$ experimentally, as a function of relaxation times. Ideally, $C_{\phi^{\pm}} \rightarrow 0$ to minimize the uncertainty in ϕ^{\pm} . Figure 4 shows that $C_{\phi^{\pm}} = 1$ for bSSFP, meaning that all the noise propagation in bSSFP transceive phase was explained by the

FIGURE 2 Accuracy of transceive phase estimation for bSSFP (first column) and PLANET (second column): results from simulations I (first row), II (second row), and III (third row). Simulation I: e_{ϕ^\pm} as a function of FA and TR; input $\Delta f_0 = 15$ Hz and $\phi^\pm = -\pi/3$ rad. Simulation II: e_{ϕ^\pm} as a function of Δf_0 and ϕ^\pm ; FA = 25° and TR = 4.6 ms. For both simulations I and II: single component with $T_1 = 832$ ms and $T_2 = 80$ ms. Simulation III: e_{ϕ^\pm} as a function of FA and TR for a 2-component voxel. First component: WM, input $\Delta f_{0,1} = 15$ Hz, $\phi_{1,1}^\pm = -\pi/3$ rad, $T_{1,1} = 832$ ms, $T_{2,1} = 80$ ms, and $w_1 = 0.88$. Second component: myelin, input $\Delta f_{0,2} = 35$ Hz (CS = 20 Hz), $\phi_{2,2}^\pm = -\pi/3$ rad, $T_{1,2} = 400$ ms, $T_{2,2} = 20$ ms, and $w_2 = 0.12$. CS, chemical shift

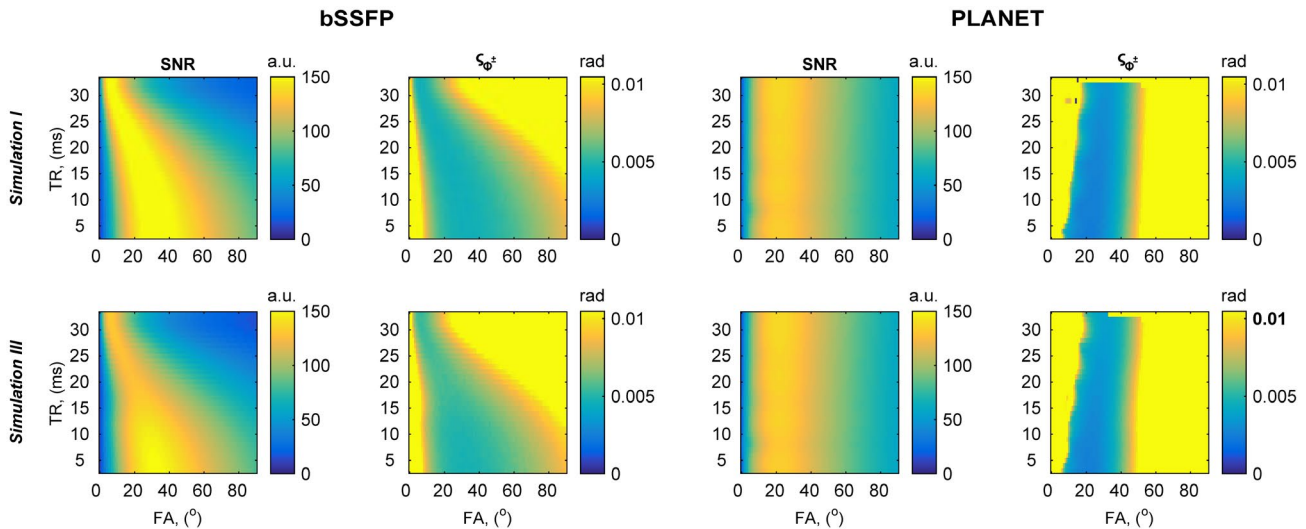
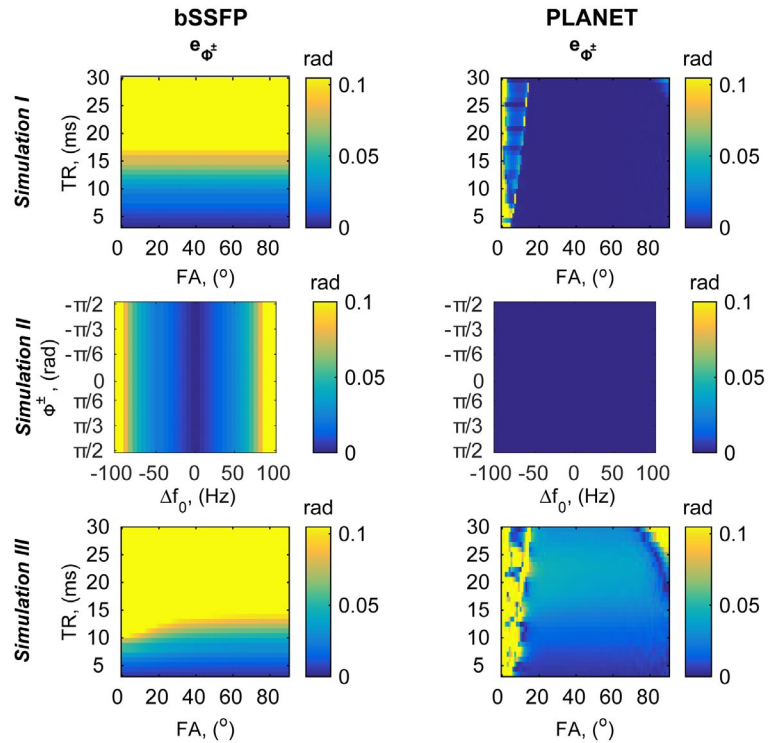


FIGURE 3 Precision of transceive phase estimation for bSSFP (left) and PLANET (right): results from simulations I (first row) and III (second row). Image SNR (as calculated in Equation 6) and the transceive phase uncertainty ζ_{ϕ^\pm} (as calculated in Equation 4) are shown as a function of FA and TR. The input parameters used for both simulation cases coincide with the ones reported in caption of Figure 2

theoretical uncertainty (Equation 5). This theoretical uncertainty holds true for phase images directly acquired from any sequence^{1,61}: a requirement fulfilled by bSSFP transceive phase. Differently, C_{ϕ^\pm} varied as a function of T_1 and T_2 in PLANET ($0.42 \leq C_{\phi^\pm} \leq 0.44$ for T_1 and T_2 of brain tissues at 3T, with FA = 25°, TR = 4.6 ms, and $N = 8$) and underlines that during PLANET processing the impact of noise on the transceive phase is approximately halved with respect to standard bSSFP. This agrees with the abovementioned ζ_{ϕ^\pm}

results found in simulation I. Based on these results, $C_{\phi^\pm}=1$ for bSSFP and $C_{\phi^\pm}=0.43$ for PLANET were used to calculate the experimental uncertainty ζ_{ϕ^\pm} (Equation 7). Figure 4 also illustrates that the constant C_{ϕ^\pm} for PLANET decreased for all three brain tissues when the number of RF phase increments was increased, showing larger values and variability for $N < 8$. On average, $0.39 \leq C_{\phi^\pm} \leq 0.50$ for $6 \leq N \leq 10$ with FA = 25° and TR = 4.6 ms. Changing N did not affect PLANET accuracy ($e_{\phi^\pm} \leq 2 \cdot 10^{-4}$ rad for any N , not shown).

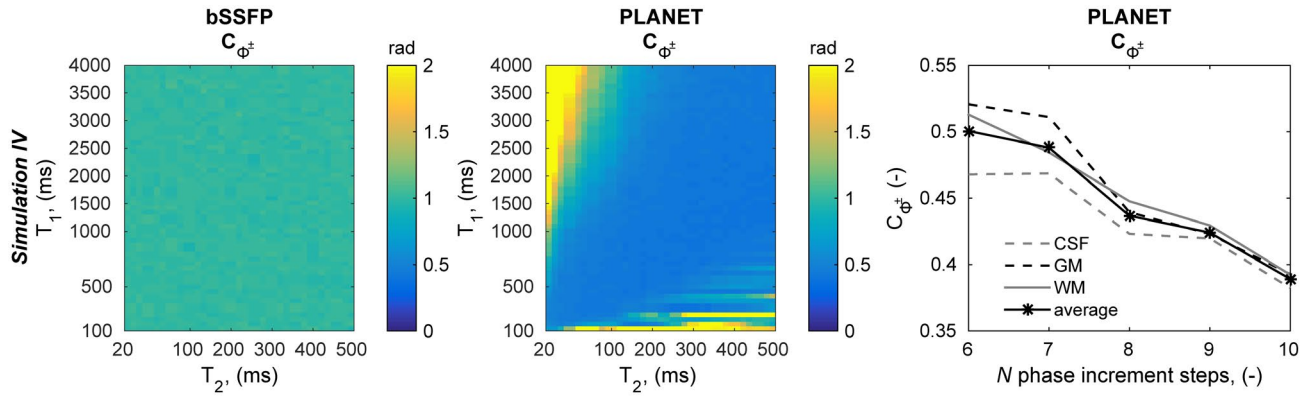


FIGURE 4 Factor $C_{\phi^{\pm}}$: results from simulation IV. $C_{\phi^{\pm}}$ maps for bSSFP (left) and PLANET (center) as a function of T_1 and T_2 . Factor $C_{\phi^{\pm}}$ for PLANET (right) as a function of N phase increment steps for CSF, GM, WM (CSF $T_1/T_2 = 3858/500$ ms, GM $T_1/T_2 = 1331/110$ ms, WM $T_1/T_2 = 832/80$ ms⁵¹) and an average among these three tissues. Simulation IV: input $\Delta f_0 = 0$ Hz, $\phi^{\pm} = -\pi/3$ rad, FA = 25°, TR = 4.6 ms, and $\Delta\theta_n = 2n\pi/N - \pi$ with $n = \{0, 1, 2, \dots, N-1\}$. $C_{\phi^{\pm}}$ maps were obtained with $N = 8$ phase increment steps. CSF, cerebrospinal fluid; GM, gray matter

4.1.4 | Simulation V

Because transient effects can compromise the accuracy of ϕ^{\pm} , predominantly in tissues with long relaxation times such as CSF, the number of RF dummy pulses should be taken into account in bSSFP and PLANET. Supporting Information Figure S3 shows that the rotation (and shape) of the fitted ellipse changed with respect to the steady state case (2500 pulses) when the number of dummy pulses was low. For our experimental settings, minimal variations in the ellipses were observed beyond 1250 dummy pulses. The transceive phase error right after 1250 dummy pulses was $3 \cdot 10^{-3}$ rad for PLANET and $1 \cdot 10^{-3}$ rad for bSSFP (Supporting Information Figure S3B). This error remained stable for bSSFP, whereas it decreased to $2 \cdot 10^{-4}$ rad for PLANET after 2500 pulses.

4.2 | Measurement results

4.2.1 | Phantom experiments

Phantom transceive phase maps are shown in Figure 5 for experiments I and II. In experiment I, a peripheral banding artefact occurred in bSSFP-based transceive phase map in the region where $\Delta f_0 > 80$ Hz (Figure 5A,L). The corresponding $\Delta\phi^{\pm}$ map displayed a spatially varying distribution, with a 0.10 rad underestimation at the phantom periphery (Figure 5J). The ϕ^{\pm} profiles in Figure 5E,L,N show that in the banding-free part of the phantom the transceive phase curvature in bSSFP was slightly smaller than in SE and PLANET, which resulted from a spurious phase contamination induced by Δf_0 (in the order of ~ 0.02 rad), as already predicted in simulation II (Figure 2). PLANET-based transceive phase map slightly underestimated the reference SE ϕ^{\pm} distribution by on average 0.03 rad (Figure 5B,K,L). A similar transceive phase map was obtained with PLANET when a linear Δf_0 variation

was enforced using the shim gradient (experiment II) (Figure 5G,M), which demonstrated the robustness of PLANET against off-resonance effects. Differently, bSSFP-based transceive phase map (after unwrapping) displayed banding artefacts in correspondence of stop-band transition regions. These artefacts could not be resolved by the unwrapping procedure (Figure 5F,M). Furthermore, both bSSFP- and PLANET-based transceive phase maps suffered from an offset (Figure 5J,K) caused by residual eddy current effects that were not fully compensated for by averaging two acquisitions with opposed readout polarity. In fact, as depicted in Supporting Information Figure S4, the linear phase accrual (along the readout direction) induced by eddy current effects in one acquisition was slightly asymmetric with respect to the phase gradient appearing in the acquisition with reversed gradient polarity. Possible reasons for this asymmetric behaviour could be small variations of Δf_0 occurring between the two acquisitions (~ 5 min apart) or slight changes in the preparatory calibration steps performed before each acquisition.

Results from experiment III, illustrated in Supporting Information Figure S5, showed that the accuracy of PLANET-based transceive phase was unaffected by the number of RF phase increments, N . In experiment III, a banding-free bSSFP transceive phase map was obtained. The corresponding Δf_0 map resembled the Δf_0 distribution of experiment I but showed a less-pronounced variation at the phantom periphery. Nevertheless, Supporting Information Figure S5K confirms that the transceive phase curvature in bSSFP was smaller than in SE, as already observed in Figure 5E,N.

The transceive phase uncertainty in PLANET was approximately half the uncertainty in bSSFP for both phantom and in vivo WM (Figure 6A). In Figure 6A, also the transceive phase uncertainty for SE is reported, which was 3 and 1.5 times higher than bSSFP uncertainty for phantom and WM, respectively. Figure 6B shows that the acquisition time

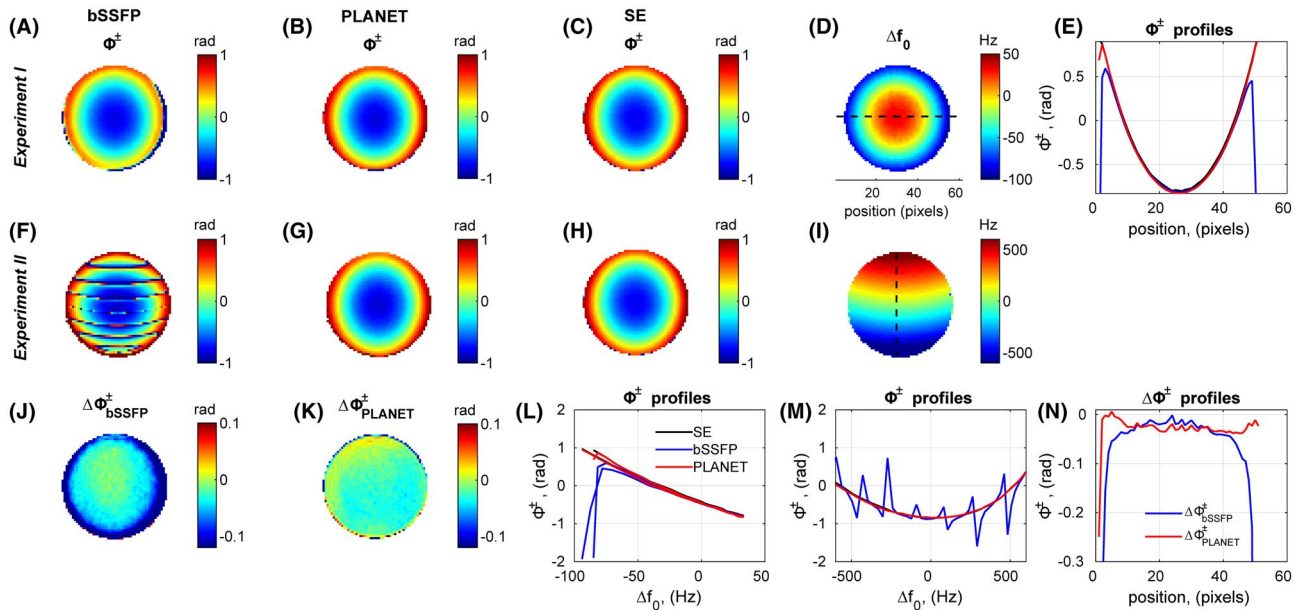


FIGURE 5 Accuracy of transceive phase estimation for bSSFP and PLANET. Results from phantom MR experiments are shown. Experiment I: volume-based shimming (A-E, J-L, N); Experiment II: linear shimming of y-gradient (F-I, M). Isotropic voxel size: 2.5 mm. Transceive phase maps (ϕ^\pm) obtained from: (A,F) bSSFP, (B,G) PLANET, and (C,H) SE (reference method) after unwrapping. (D,I) Δf_0 maps. (E) Transceive phase profiles of bSSFP (blue), PLANET (red), and SE (black), calculated on the central horizontal line (dashed line in (D)) for experiment I. (J) $\Delta\phi^\pm$ for bSSFP, defined as $\phi_{bSSFP}^\pm - \phi_{SE}^\pm$, based on transceive phase maps (A) and (C). (K) $\Delta\phi^\pm$ for PLANET, defined as $\phi_{PLANET}^\pm - \phi_{SE}^\pm$, based on transceive phase maps (B) and (C). (L) Transceive phase profiles, calculated on the central horizontal line (dashed line in (D)), as a function of Δf_0 for experiment I (A-D). (M) Transceive phase profiles, calculated on the central vertical line (dashed line in (I)), as a function of Δf_0 for experiment II (F-I). The legend is the same as in (L). (N) $\Delta\phi^\pm$ profiles for $\Delta\phi^\pm_{bSSFP}$ (blue) and $\Delta\phi^\pm_{PLANET}$ (red) calculated on the central horizontal line (dashed line in (D)) for experiment I. SE, spin echo

of phase-cycled bSSFP needed for PLANET was longer than bSSFP of a factor N (in this case, $N = 8$). Still, this time was 2 min faster than SE acquisition. Using the ζ_{ϕ^\pm} reported in Figure 6A for WM and the scan time in Figure 6B, we calculated the precision-per-unit-time ($(\zeta_{\phi^\pm} \cdot t)^{-1}$) shown in Figure 6C: the precision-per-unit-time for PLANET was 4 times lower than for bSSFP and 8.5 times higher than for SE.

The ζ_{ϕ^\pm} trends in the phantom (Figure 6A) were also reflected in the conductivity maps presented in Figures 7 and S5: SE-based conductivity map was visually noisier than bSSFP-based and PLANET-based conductivity maps, whereas PLANET-based conductivity appeared least noisy. Quantitatively, the lowest conductivity SD was found in PLANET, although the conductivity SD values were of the same order of magnitude in all methods. Similarly, a rather mild decrease of conductivity SD with increasing N was found in Supporting Information Figure S5, which is line with the simulated trend of C_{ϕ^\pm} portrayed in Figure 4. Moreover, in all conductivity maps, the effect of Gibbs ringing at phantom periphery was amplified. In both Figure 7 and Supporting Information Figure S5, the median values (reported in the boxplot) for both PLANET-based and SE-based conductivity were close to the true value. In bSSFP, the median conductivity was underestimated in both experiments I and III, which was caused by the aforementioned smaller curvature of the observed transceive phase.

4.2.2 | In vivo brain experiments

Transceive phase and conductivity results for volunteer 1 are presented in Figures 8 and 9, and Supporting Information Figure S6. Figure 8 highlights that PLANET reconstructed T_1 , T_2 , and Δf_0 maps, besides ϕ^\pm . The transceive phase maps from bSSFP and PLANET globally resembled the reference SE map (Figure 8). Maps for ζ_{ϕ^\pm} showed larger uncertainty in SE, which agreed with the phantom data (Figure 6). The $\Delta\phi^\pm$ maps in Figure 9 did reveal a smoother distribution in PLANET than in bSSFP. In particular, perturbations in bSSFP were observed, for example, near the genu of corpus callosum in the frontal lobe ($\Delta\phi^\pm > 0.04$ rad) and in the posterior lobe. The error in proximity of the corpus callosum could be associated with Δf_0 , which rapidly exceeded 50 Hz ($\approx \frac{1}{4TR}$), and cardiac pulsation transferred to the neighbouring CSF.⁶³ The origin of the slight artefact in the right posterior lobe is unclear; this artefact, nevertheless, was absent in PLANET (Figure 8D). Moreover, in both methods a residual phase accumulation (with a peak value of ~ 0.06 rad) was found in the left side of the frontal lobe (Figure 9). Similarly to the phantom case, this residual phase appeared because the asymmetric linear phase gradients induced by eddy currents in both acquisitions did not completely cancel out when averaging was performed (Supporting Information

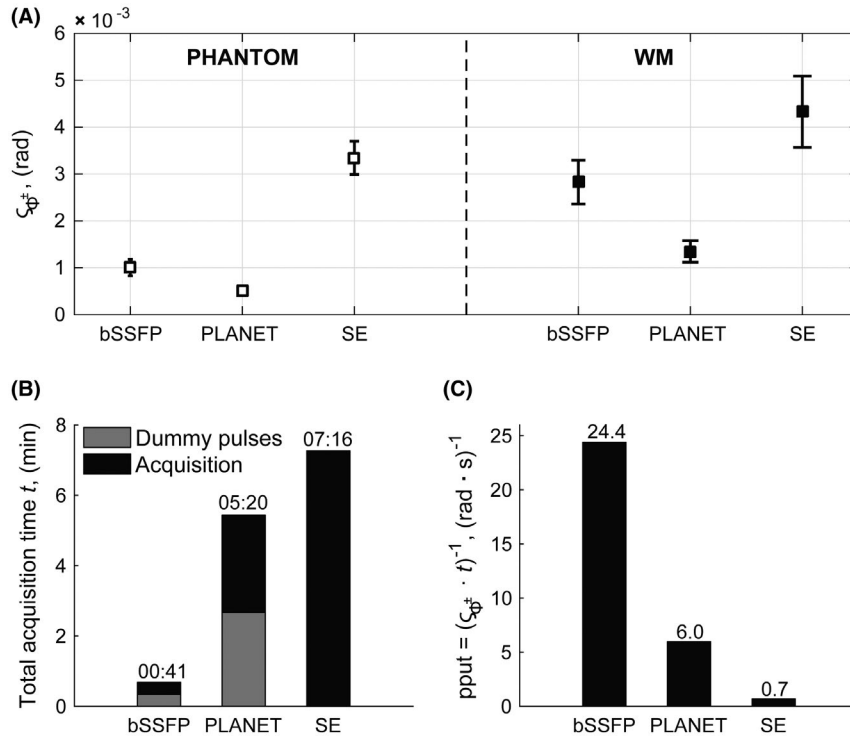


FIGURE 6 Precision, acquisition time, and precision-per-unit-time of transceive phase estimation for bSSFP, PLANET, and SE. A, Transceive phase precision: mean values of transceive phase uncertainty $\zeta_{\phi_{\pm}}$ are reported along with the SD (error bars). Isotropic voxel size: 2.5 mm. The transceive phase uncertainty $\zeta_{\phi_{\pm}}$ was calculated with Equation 7 in the phantom (*empty square*) and in WM (*full square*) of volunteer 3 ($C_{\phi_{\pm}}=1$ for bSSFP and SE, $C_{\phi_{\pm}}=0.43$ for PLANET). WM was segmented using MICO segmentation method.⁷⁰ Voxels of the central slice were used for $\zeta_{\phi_{\pm}}$ calculation in both cases. B, Total acquisition time for the three methods (i.e., including both acquisitions with opposite readout gradient polarity). In bSSFP and PLANET, the time spent for both the dummy pulses and the actual acquisition is shown (a series of ~2170 dummy RF pulses, corresponding to ~10 s, was added before each phase-cycled bSSFP acquisition). C, Precision-per-unit-time for the three methods, calculated as $(\zeta_{\phi_{\pm}} \cdot t_i)^{-1}$, by using $\zeta_{\phi_{\pm}}$ values for WM in (A) and the total time t_i in (B). MICO, multiplicative intrinsic component optimization; pput, precision-per-unit-time

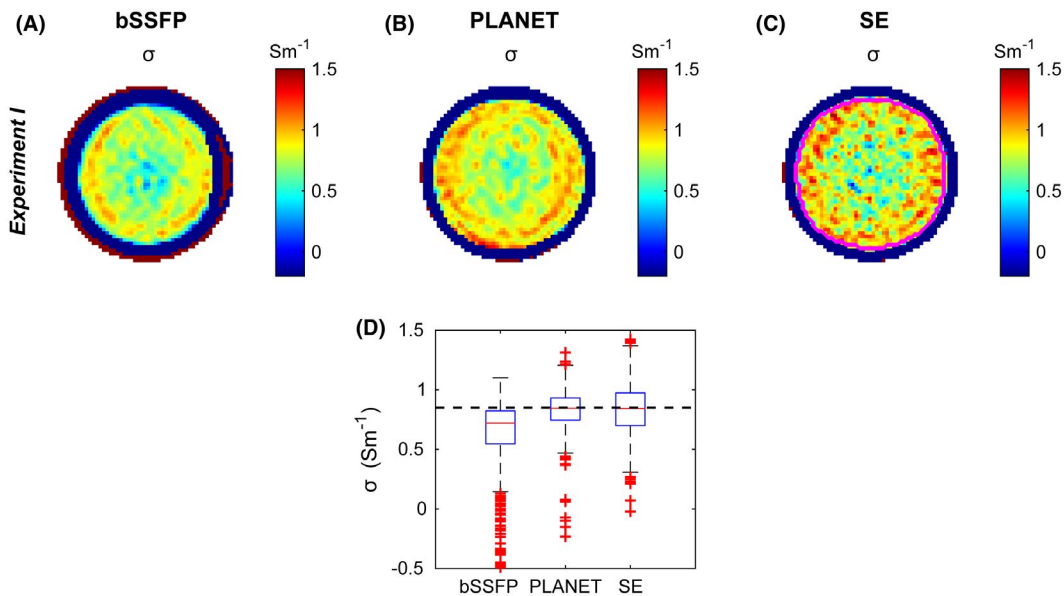


FIGURE 7 Phantom conductivity based on bSSFP, PLANET, and SE (reference) methods from experiment I. Conductivity maps reconstructed from transceive phase maps estimated with A, bSSFP, B, PLANET, and C, SE in experiment I. The transceive phase maps used for conductivity reconstruction are shown in Figure 5 (A-C). D, Boxplot of conductivity values, evaluated in the circular ROI (shown in magenta color in (C)) in the central slice of the phantom. The ROI was based on thresholding on SE magnitude image followed by erosion to exclude EPT boundary errors. The true conductivity value, as measured by the dielectric probe, is shown with a black dashed line. EPT, electrical properties tomography; ROI, region of interest

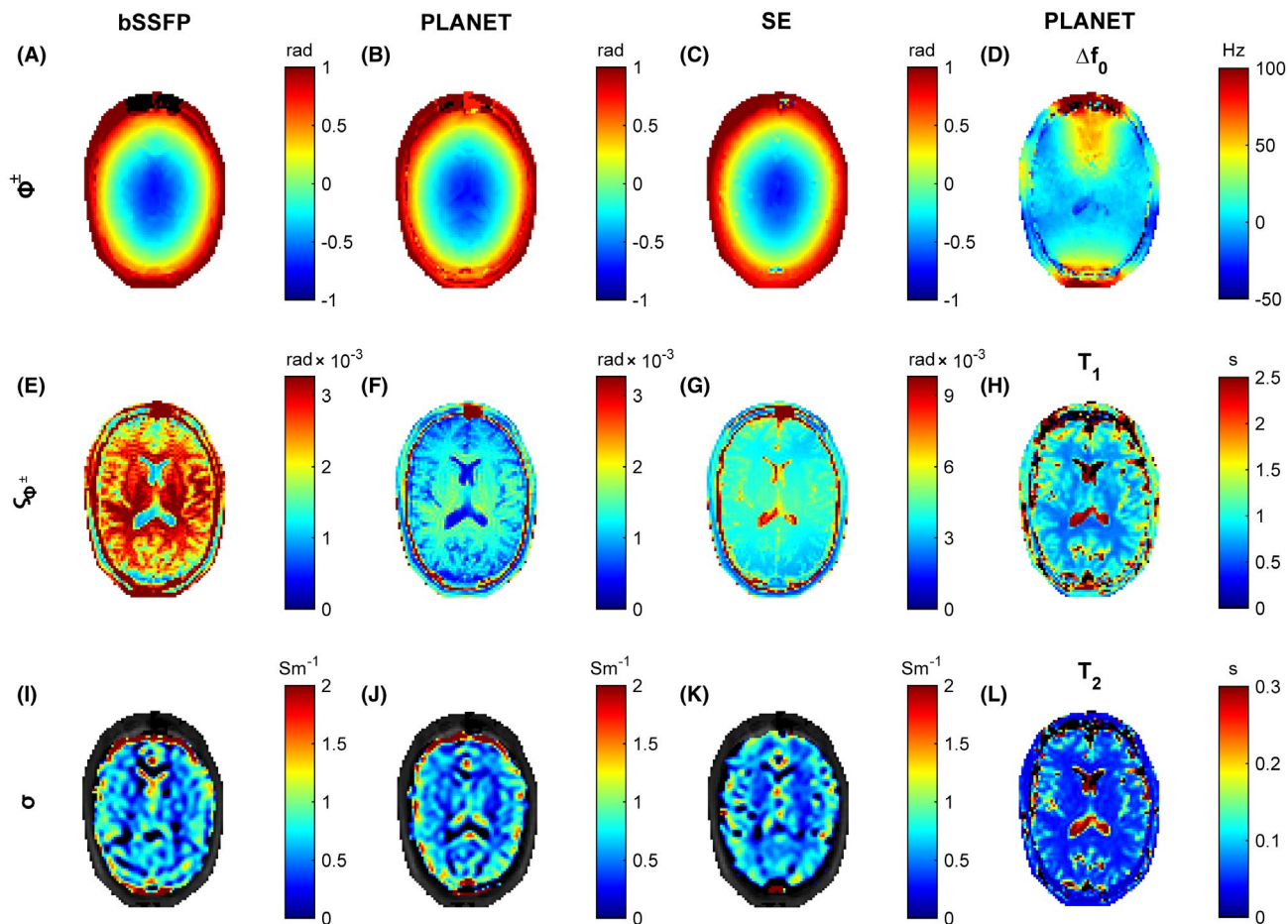


FIGURE 8 In vivo brain results for volunteer 1, obtained with bSSFP (first column), PLANET (second column), and SE (reference, third column) methods. Isotropic voxel size: 2.5 mm. Transceive phase maps (ϕ^\pm) obtained from (A) bSSFP, (B) PLANET, and (C) SE after unwrapping. (D) Δf_0 map obtained with PLANET. Maps of the transceive phase uncertainty (ς_{ϕ^\pm}) for (E) bSSFP, (F) PLANET, and (G) SE. The ς_{ϕ^\pm} for SE was calculated with Equation 7, $C_{\phi^\pm} = 1$, being SE-based ϕ^\pm -map directly acquired. Note the different colorbar in (G) with respect to (E) and (F). (H) T_1 map obtained with PLANET. Conductivity maps based on (I) bSSFP, (J) PLANET, and (K) SE, reconstructed from transceive phase maps shown in (A-C) respectively. (L) T_2 map obtained with PLANET. Note that T_1 and T_2 maps are expected to suffer a $\sim 20\%$ to 25% bias because the TR used in this study (4.6 ms) was specifically chosen for transceive phase mapping but was suboptimal for T_1 and T_2 mapping⁴⁷

Figure S6). Supporting Information Figure S6 also shows that Helmholtz-based conductivity maps reconstructed on the single acquisition with one gradient polarity differed slightly from the conductivity map retrieved from their average (as already observed in the phantom, Supporting Information Figure S4). However, for all methods the conductivity maps had comparable quality and enhanced the errors present in the corresponding transceive phase maps, as expected. Distortions in bSSFP conductivity were found in correspondence of the abovementioned locations (Figure 8I and $\Delta\sigma$ in Figure 9). The SE-based conductivity exhibited errors in proximity of vessels, attributed to inflow artefacts appearing in its underlying transceive phase map (due to SE 2D spatial encoding). All conductivity maps showed errors in CSF; these were more prominent for bSSFP and PLANET, likely because of mild phase disturbances caused by CSF pulsation.⁶³ Similar results were

observed for the other volunteers (Supporting Information Figure S7). In volunteer 2, nonetheless, bSSFP- and PLANET-based conductivity maps were almost alike (Supporting Information Figure S7E,F). Interestingly, less spatial fluctuations were found in bSSFP-based ϕ^\pm and $\Delta\phi^\pm$ maps, and a smooth Δf_0 map was acquired, the values of which were within the pass-band region (Supporting Information Figure S7H).

5 | DISCUSSION

In this study, we introduced a novel technique to map the transceive phase ϕ^\pm , the PLANET method, an ellipse fitting approach to phase-cycled bSSFP data. We studied accuracy and precision of its ϕ^\pm estimates in brain with simulations and MR measurements and compared these to ϕ^\pm acquired

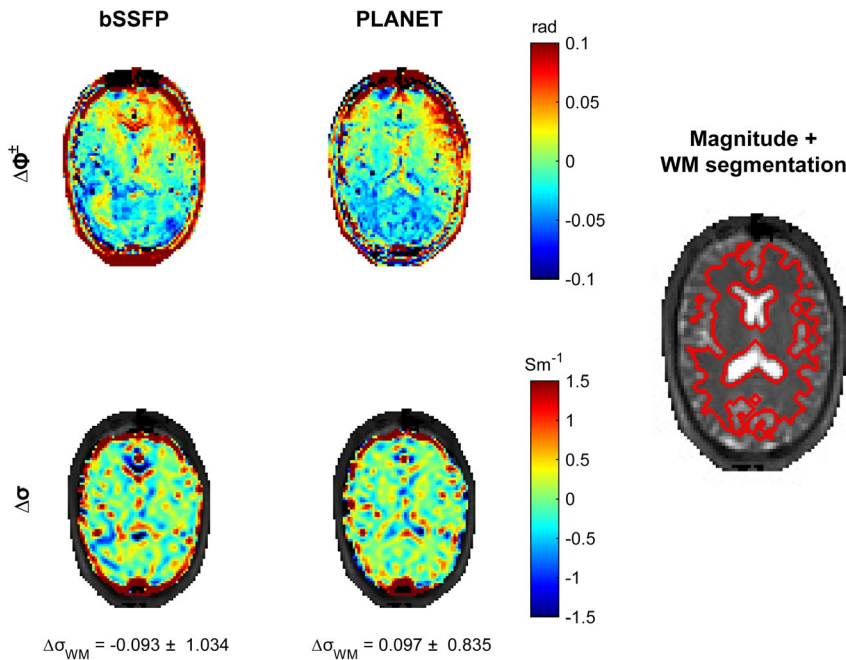


FIGURE 9 Transceive phase difference maps ($\Delta\phi^\pm$, top) and conductivity difference maps ($\Delta\sigma$, bottom) for both bSSFP (left) and PLANET (right) for volunteer 1. Difference maps were performed with respect to SE-based ϕ^\pm and σ ($\Delta\phi^\pm_{bSSFP/PLANET} = \phi^\pm_{bSSFP/PLANET} - \phi^\pm_{SE}$ and $\Delta\sigma_{bSSFP/PLANET} = \sigma_{bSSFP/PLANET} - \sigma_{SE}$). Transceive phase and conductivity maps are shown in Figure 8. Mean \pm SD $\Delta\sigma$ values in WM are reported below the corresponding map. WM segmentation was performed with MICO segmentation method⁷⁰ and is shown in red on the banding-free magnitude image obtained with PLANET method

with standardly used transceive phase mapping sequences (bSSFP and SE). To the best of the authors' knowledge, this is the first study comparing transceive phase mapping methods. Furthermore, based on experimental ϕ^\pm maps, we reconstructed Helmholtz-based conductivity maps to provide an example of an application that depends on transceive phase information. Our analysis demonstrated that PLANET can reconstruct accurate and precise transceive phase maps in the brain, therefore allowing reliable reconstruction of brain tissue conductivity.

A fundamental benefit offered by the PLANET method is that it retrieves transceive phase maps free from off-resonance effects that generally contaminate the transceive phase acquired with bSSFP. The superior robustness of PLANET against off-resonance variations was proven in both simulations (Figure 2 and Supporting Information Figure S1) and phantom measurements (Figure 5 and Supporting Information Figure S5) and is particularly advantageous for large off-resonances, which result in banding artefacts in bSSFP-based transceive phase (see, for example, experiment II, when a linear field variation was artificially induced) (Figure 5F-I). This different robustness against off-resonance effects depends on how both methods estimate ϕ^\pm : as detailed in the Theory section, in standard bSSFP the signal phase is commonly associated with the transceive phase. Considering that the signal phase $\angle I_0 = \angle(1 - E_2 e^{-i(\theta_0 + \pi)}) \cdot e^{i\Omega}$ is mainly influenced by the transceive phase (in Ω), the off-resonance (in Ω and θ_0), and T_2 (in E_2), the equivalence $\phi^\pm =$ signal phase is a suitable approximation when all other phase contributions are negligible. Banding artefacts and T_2 effects, for instance, occur when $|\Delta f_0| > (3 \text{ TR})^{-1}$.⁴⁴ Ideally, these effects could be eliminated by combining appropriate B_0 shimming

with short TRs, two options that depend on the available MR system's hardware and software tools and the imaged object. Within the pass-band region, however, bSSFP-based ϕ^\pm can still be contaminated by Δf_0 -induced "phase leakage," which can mildly modify ϕ^\pm curvature (e.g., Figure 5E,J,N and Supporting Information Figure S5K). Differently, in PLANET the transceive phase is intrinsically corrected for Δf_0 (and T_2) effects because it results directly from the difference between the off-resonance-driven phase and the rotation angle Ω (Equation 2), and these two parameters are estimated independently from the shape of the ellipse.

Besides PLANET, other techniques have been proposed specifically to remove bandings from bSSFP transceive phase. A postprocessing pipeline for 2D phase unbanding was reported by Kim et al.⁴⁵ The recent correction technique by Ozdemir and Ider⁴⁴ relies on two bSSFP dynamics with a $(2 \text{ TR})^{-1}$ frequency shift, which is conceptually similar to employing a phase-cycling scheme. Their methodology does require extra Δf_0 and T_2 measurements to correct bSSFP-based ϕ^\pm for the abovementioned effects, thus elongating the total scanning time to > 15 min. Compared with this last technique, PLANET bypasses the need for additional acquisitions because it estimates simultaneously ϕ^\pm , Δf_0 , T_2 , and T_1 within shorter times⁴⁸ (Figure 8).

Shcherbakova et al.⁴⁷ have already shown that accuracy and precision in T_1 and T_2 in WM estimated with PLANET depend on appropriate selection of sequence settings. Similarly, our simulation results demonstrated that the choice of FA, TR, and N (number of RF phase increments) influence the accuracy and precision of PLANET transceive phase estimates. Unsurprisingly, increasing N benefitted the transceive phase precision (Figure 4) at the cost of longer acquisition

times. Unlike when optimizing T_1 and T_2 accuracy,⁴⁷ using $TR < 10$ ms was beneficial for transceive phase accuracy in PLANET, but mostly in bSSFP, especially when a second component such as myelin was present in the voxel (Figure 2 and Supporting Information Figure S1). The FA choice was relevant for the precision: in both PLANET and bSSFP, the lowest uncertainty (ζ_{ϕ^\pm}) was found for $FA = [20-30]^\circ$ (Figure 3 and Supporting Information Figure S2). Hence, FA and TR should be carefully selected in voxels with mixed content.

Based on all simulation predictions for ϕ^\pm , we selected $FA = 25^\circ$, $TR = 4.6$ ms, and $N = 8$ for all our MR measurements. We also acquired and averaged 2 phase maps obtained with identical settings but reversed readout gradient polarity in order to reduce the impact of eddy currents on the transceive phase. In the volunteer study, both PLANET and bSSFP showed similar $\Delta\phi^\pm$ spatial distributions, with mild perturbations in WM. Besides residual errors caused by eddy currents effects in both methods and by off-resonance effects in bSSFP (which we have already discussed), we hypothesize that bias in WM, albeit small, could originate from partial volume that is likely to occur for the voxel size chosen (2.5 mm isotropic). This is supported by the fact that multiple species with different susceptibilities or chemical shifts are present in human WM (e.g., myelin, proteins, lipids, iron, deoxyhemoglobin).^{52,64} Characterizing the effect of such species in the transceive phase estimated with PLANET or bSSFP was beyond the scope of this study, but the example of a common 2-component relaxation model for human brain (i.e., WM as dominant component and myelin as second component) reported in Figure 2 and Supporting Information Figure S1 already demonstrated that myelin properties caused errors in both methods, with bSSFP being increasingly more sensitive than PLANET to myelin presence when the dominant component was no longer on resonance. These errors, as already explained by, for example, Miller⁶⁵ and Miller et al.,⁵² arise because multiple components with different frequency distribution within the same voxel distort the symmetry of bSSFP profile. As a result, in phase-cycled bSSFP data these asymmetries can modify rotation and shape of the ellipse corresponding to the main signal (dominant WM component) on which PLANET fitting is applied.⁴⁷

Besides the aforementioned lower sensitivity to off-resonance effects and partial volume, we observed a lower ζ_{ϕ^\pm} for PLANET than for bSSFP and SE (of a factor 2 and 3, respectively, for our sequence settings) (Figure 6A). Nonetheless, the acquisition of phase-cycled bSSFP data needed for PLANET was 8 times slower than the standard bSSFP acquisition (because $N = 8$). Thus, the precision-per-unit-time was higher for bSSFP than for PLANET: overall, bSSFP was 4 times more efficient than PLANET (Figure 6C). Note also that if precision in the transceive phase were of primary importance rather than accuracy, averaging 8 standard bSSFP acquisitions would produce

a $2\sqrt{2}$ precision increase in ϕ^\pm , which is $\sqrt{2}$ times higher than the precision gain obtained in PLANET-based transceive phase with respect to single bSSFP-based transceive phase. In brain experiments, however, acquiring two phase-cycled bSSFP scans with opposed gradient polarity was 2 min faster than the conventional SE and took in total 5 min, a duration we deemed (already) clinically acceptable, especially in light of the simultaneous reconstruction of T_1 , T_2 , Δf_0 . Although we did not consider accelerating the acquisition in this work, decreasing the number of dummy pulses and the number of RF phase increments N might serve this purpose. For example, decreasing the number of dummy pulses from ~ 2100 to ~ 1300 would save ~ 1 min for our sequence settings, at the cost of reduced accuracy in all parameters reconstructed with PLANET.⁴⁷ However, the resulting transceive phase error would be rather small ($e_{\phi^\pm} \approx 2.7 \cdot 10^{-3}$ rad) (Supporting Information Figure S3). Reducing N to the minimum ($N = 6$) would additionally shorten the acquisition by 1:20 min (corresponding to -25% of the total time reported in Figure 6B) and a $\sim 15\%$ reduction in transceive phase precision would be paid (Figure 4). Furthermore, using acceleration techniques such as parallel imaging (e.g., SENSE⁶⁶) or compressed sensing (e.g., ref. 67) would also be recommendable, but their effect on transceive phase reconstruction should be critically evaluated.

An example of an application for which accurate transceive phase maps are important is conductivity mapping with EPT, and precise maps are especially indicated for differentiation-based EPT methods, which are typically more sensitive to noise than integration-based methods.¹⁶ Although multiple EPT reconstruction methods to map brain conductivity have been proposed previously (e.g., references 11,14,15,19,22), here we employed the conventional (phase-only) Helmholtz-based approach because of its known linear noise propagation from transceive phase to conductivity⁶⁸ that allows comparison of ϕ^\pm mapping methods. In the homogeneous phantom, the conductivity SD was on the same order of magnitude for all methods, despite their different ζ_{ϕ^\pm} . This reveals a low linear coefficient (or slope) in the abovementioned noise propagation relationship of this EPT method and is in line with the theoretical model by Lee et al.⁶⁸ PLANET and SE had comparable median conductivity values, whereas bSSFP underestimated the conductivity because of a slightly altered shape of its transceive phase (Figure 7 and Supporting Information Figure S5). Our conductivity findings also suggest that the acquisition duration could be more than halved in PLANET (from $\sim 05:20$ min with the settings used in this study to 02:03 min) if conductivity retrieval alone were of interest, because mapping ϕ^\pm from a single polarity acquisition (Supporting Information Figures S4 and S6, both PLANET and bSSFP) and reducing N to 6 for PLANET (Supporting Information Figure S5) had little impact on the accuracy and precision

of Helmholtz-based conductivity. Nonetheless, whether this impact remains little for conductivity maps obtained with other EPT methods should be verified. In vivo, the small disturbances present in transceive phase maps of PLANET, bSSFP and also SE were unsurprisingly enhanced in the corresponding conductivity maps. Overall, PLANET-based conductivity qualitatively resembled the reference SE-based conductivity for all volunteers (Figure 8 and Supporting Information Figure S7). Thus, we expect that using any other EPT reconstruction algorithms on PLANET-based transceive phase map would produce conductivity maps at least comparable to the conductivity maps reconstructed with presently used sequences.

6 | CONCLUSION

The newly introduced PLANET method reconstructs accurate and precise transceive phase maps when appropriate sequence settings are chosen and is therefore a valid technique to map brain transceive phase and conductivity. PLANET retrieves transceive phase maps free from off-resonances effects, which typically corrupt bSSFP maps. This renders PLANET suitable for situations in which stronger B_0 inhomogeneity comes into play (e.g., for field strengths >1.5 T) and/or with limited B_0 shimming control. Furthermore, sensitivity to partial volume effects is better attenuated in PLANET than in bSSFP. Despite its longer acquisition time and lower time-efficiency than bSSFP, PLANET simultaneously retrieves banding-free magnitude image, T_1 , T_2 , Δf_0 ,⁴⁸ and transceive phase and can be exploited for reconstruction of conductivity and magnetization transfer parameters⁶⁹ within clinically feasible times, which could be useful for quantitative brain tissue characterization.

ACKNOWLEDGMENT

We thank Stefano Mandija for his help in building the phantom and for fruitful discussions.

ORCID

Soraya Gavazzi  <https://orcid.org/0000-0003-4298-0353>

Yulia Shcherbakova  <https://orcid.org/0000-0003-3521-1767>

REFERENCES

- Haacke EM, Brown RW, Thompson MR, Venkatesan R. *Magnetic Resonance Imaging: Physical Principles and Sequence Design*, 1st ed. New York, NY: John Wiley & Sons; 1999.
- Hoult DI. The principle of reciprocity in signal strength calculations? *A mathematical guide. Concept Magn Reson.* 2000;12:173–187.
- Vaidya MV, Collins CM, Sodickson DK, Brown R, Wiggins GC, Lattanzi R. Dependence of B1– and B1+ field patterns of surface coils on the electrical properties of the sample and the MR operating frequency. *Concepts Magn Reson Part B Magn Reson Eng.* 2016;46:25–40.
- Bottomley PA, Andrew ER. RF magnetic field penetration, phase shift and power dissipation in biological tissue: implications for NMR imaging. *Phys Med Biol.* 1978;23:006.
- Collins CM, Li S, Smith MB. SAR and B1 field distributions in a heterogeneous human head model within a birdcage coil. *Magn Reson Med.* 1998;40:847–856.
- Yang QX, Wang J, Zhang X, et al. Analysis of wave behavior in lossy dielectric samples at high field. *Magn Reson Med.* 2002;47:982–989.
- Collins CM, Liu W, Schreiber W, Yang QX, Smith MB. Central brightening due to constructive interference with, without, and despite dielectric resonance. *J Magn Reson Imaging.* 2005;21:192–196.
- Van de Moortele P-F, Akgun C, Adriani G, et al. B1 destructive interferences and spatial phase patterns at 7 T with a head transceiver array coil. *Magn Reson Med.* 2005;54:1503–1518.
- Katscher U, Findekle C, Voigt T. B1-based specific energy absorption rate determination for nonquadrature radiofrequency excitation. *Magn Reson Med.* 2012;68:1911–1918.
- Wen H. Noninvasive quantitative mapping of conductivity and dielectric distributions using RF wave propagation effects in high field MRI. In: Yaffe MJ, Antonuk LE, eds. *Proceedings of the SPIE, Volume 5030, Medical Imaging: Physics of Medical Imaging.* International Society for Optics and Photonics; 2003. p. 471–477.
- Voigt T, Katscher U, Doessel O. Quantitative conductivity and permittivity imaging of the human brain using electric properties tomography. *Magn Reson Med.* 2011;66:456–466.
- Leijssen RL, Brink WM, van den Berg C, Webb AG, Remis RF. 3-D contrast source inversion-electrical properties tomography. *IEEE Trans Med Imaging.* 2018;37:2080–2089.
- Serralles JEC, Giannakopoulos I, Zhang B, et al. Noninvasive estimation of electrical properties from magnetic resonance measurements via global Maxwell tomography and match regularization. *IEEE Trans Biomed Eng.* 2019;1.
- Gurler N, Ider YZ. Gradient-based electrical conductivity imaging using MR phase. *Magn Reson Med.* 2017;77:137–150.
- Hafalir FS, Oran OF, Gurler N, Ider YZ. Convection-reaction equation based magnetic resonance electrical properties tomography (cr-MREPT). *IEEE Trans Med Imaging.* 2014;33:777–793.
- Katscher U, van den Berg C. Electric properties tomography: Biochemical, physical and technical background, evaluation and clinical applications. *NMR Biomed.* 2017;30:e3729.
- Katscher U, Voigt T, Findekle C, Vernickel P, Nehrke K, Dössel O. Determination of electric conductivity and local SAR via B1 mapping. *IEEE Trans Med Imaging.* 2009;28:1365–1374.
- Liu J, Wang Y, Katscher U, He B. Electrical properties tomography based on B1 maps in MRI: principles, applications, and challenges. *IEEE Trans Biomed Eng.* 2017;64:2515–2530.
- van Lier A, Brunner DO, Pruessmann KP, et al. B1+ phase mapping at 7 T and its application for in vivo electrical conductivity mapping. *Magn Reson Med.* 2012;67:552–561.
- Shin J, Kim J-H, Kim D-H. Redesign of the Laplacian kernel for improvements in conductivity imaging using MRI. *Magn Reson Med.* 2019;81:2167–2175.

21. van Lier A, Raaijmakers A, Voigt T, et al. Electrical properties tomography in the human brain at 1.5, 3, and 7T: A comparison study. *Magn Reson Med.* 2014;71:354–363.
22. Hampe N, Herrmann M, Amthor T, Findeklee C, Doneva M, Katscher U. Dictionary-based electric properties tomography. *Magn Reson Med.* 2019;81:342–349.
23. Katscher U, Djamshidi K, Voigt T, et al. Estimation of breast tumor conductivity using parabolic phase fitting. In Proceedings of the 20th Annual Meeting of ISMRM, Melbourne, Australia, 2012. p. 3482.
24. Shin J, Kim MJ, Lee J, et al. Initial study on in vivo conductivity mapping of breast cancer using MRI. *J Magn Reson Imaging.* 2015;42:371–378.
25. Stehning C, Voigt T, Karkowski P, Katscher U. Electric properties tomography (EPT) of the liver in a single breathhold using SSFP. In Proceedings of the 20th Annual Meeting of ISMRM, Melbourne, Australia, 2012. p. 386.
26. Balidemaj E, van Lier ALHMW, Crezee H, Nederveen AJ, Stalpers LJA, van den Berg CAT. Feasibility of electric property tomography of pelvic tumors at 3T. *Magn Reson Med.* 2015;73:1505–1513.
27. Tha KK, Katscher U, Yamaguchi S, et al. Noninvasive electrical conductivity measurement by MRI: a test of its validity and the electrical conductivity characteristics of glioma. *Eur Radiol.* 2018;28:348–355.
28. Mori N, Tsuchiya K, Sheth D, et al. Diagnostic value of electric properties tomography (EPT) for differentiating benign from malignant breast lesions: comparison with standard dynamic contrast-enhanced MRI. *Eur Radiol.* 2019;29:1778–1786.
29. Balidemaj E, Kok HP, Schooneveldt G, et al. Hyperthermia treatment planning for cervical cancer patients based on electrical conductivity tissue properties acquired in vivo with EPT at 3 T MRI. *Int J Hyperthermia.* 2016;32:558–568.
30. Crezee J, Bennis M, Gavazzi S, Stalpers L, van Lier ALHMW, Kok HP. Development of electrical properties tomography for hyperthermia treatment planning. In Proceedings of the First IEEE MTT-S International Microwave Bio Conference (IMBIOC), Gothenburg Sweden, 2017. p. 1–4.
31. Mandija S, Petrov PI, Neggens S, Luijten PR. Noninvasive electric current induction for low-frequency tissue conductivity reconstruction: is it feasible with a TMS-MRI setup? *Tomography.* 2016;2:203–214.
32. Peters RD, Henkelman RM. Proton-resonance frequency shift MR thermometry is affected by changes in the electrical conductivity of tissue. *Magn Reson Med.* 2000;43:62–71.
33. Salim G, Baron P, Poot D, et al. Effect of the transceive phase on MR thermometry in aqueous mediums. In Proceedings of the 25th Annual Meeting of ISMRM, Honolulu, HI, 2017. p. 5422.
34. Kim DH, Choi N, Gho SM, Shin J, Liu C. Simultaneous imaging of in vivo conductivity and susceptibility. *Magn Reson Med.* 2014;71:1144–1150.
35. Robinson SD, Bredies K, Khabipova D, Dymerska B, Marques JP, Schweser F. An illustrated comparison of processing methods for MR phase imaging and QSM: combining array coil signals and phase unwrapping. *NMR Biomed.* 2017;30:e3601.
36. Schweser F, Huang L, Hermann K-H, Krmer M, Deistung A, Reichenbach JR. Conductivity mapping using ultrashort echo time (UTE) imaging. In Proceedings of the 21st Annual Meeting of ISMRM, Salt Lake City, UT, 2013. p. 4190.
37. Lee SK, Bulumulla S, Wiesinger F, Sacolick L, Sun W, Hancu I. Tissue electrical property mapping from zero echo-time magnetic resonance imaging. *IEEE Trans Med Imaging.* 2015;34:541–550.
38. Weiger M, Pruessmann KP. MRI with zero echo time. In: Grant DM, Harris RK. *Encyclopedia of Magnetic Resonance: EMR.* Chichester, UK: John Wiley & Sons; 2012.
39. Stehning C, Voigt T, Katscher U. Real time conductivity mapping using balanced SSFP and phase based reconstruction. In Proceedings of the 19th Annual Meeting of ISMRM, Montréal, Québec, Canada, 2011. p. 128.
40. Xiang QS, Hoff MN. Banding artifact removal for bSSFP imaging with an elliptical signal model. *Magn Reson Med.* 2014;71:927–933.
41. Björk M, Ingle RR, Gudmundson E, Stoica P, Nishimura DG, Barral JK. Parameter estimation approach to banding artifact reduction in balanced steady-state free precession. *Magn Reson Med.* 2014;72:880–892.
42. Bangerter NK, Hargreaves BA, Vasanawala SS, Pauly JM, Gold GE, Nishimura DG. Analysis of multiple-acquisition SSFP. *Magn Reson Med.* 2004;51:1038–1047.
43. Lauzon ML, Frayne R. Analytical characterization of RF phase-cycled balanced steady-state free precession. *Concepts Magn Reson Part A.* 2009;34A:133–143.
44. Ozdemir S, Ider YZ. bSSFP phase correction and its use in magnetic resonance electrical properties tomography. *Magn Reson Med.* 2019;81:934–946.
45. Kim M-O, Choi N, Shin J, Lee J, Kim D-H. Phase unbanding in bSSFP for liver conductivity imaging at 3.0T. In Proceedings of the 21st Annual Meeting of ISMRM, Salt Lake City, UT, 2013. p. 4173.
46. Gavazzi S, Shcherbakova Y, Mandija S, et al. Sequences for transceive phase mapping: a comparison study and application to conductivity imaging. In Proceedings of the 26th Annual Meeting of ISMRM, Paris, France, 2018. p. 5084.
47. Shcherbakova Y, van den Berg C, Moonen C, Bartels LW. On the accuracy and precision of PLANET for multiparametric MRI using phase-cycled bSSFP imaging. *Magn Reson Med.* 2019;81:1534–1552.
48. Shcherbakova Y, van den Berg C, Moonen C, Bartels LW. PLANET: an ellipse fitting approach for simultaneous T1 and T2 mapping using phase-cycled balanced steady-state free precession. *Magn Reson Med.* 2018;79:711–722.
49. Bieri O, Scheffler K. Fundamentals of balanced steady state free precession MRI. *J Magn Reson Imaging.* 2013;38:2–11.
50. Hargreaves B. Bloch equation simulator. Available at: <http://mrsrl.stanford.edu/~brian/blochsim/>. Accessed January 15, 2019.
51. Wansapura JP, Holland SK, Dunn RS, Ball WS. NMR relaxation times in the human brain at 3.0 Tesla. *J Magn Reson Imaging.* 1999;9:531–538.
52. Miller KL, Smith SM, Jezzard P. Asymmetries of the balanced SSFP profile. Part II: White matter. *Magn Reson Med.* 2010;63:396–406.
53. Alonso-Ortiz E, Levesque IR, Pike GB. MRI-based myelin water imaging: A technical review. *Magn Reson Med.* 2015;73:70–81.
54. Rioux JA, Levesque IR, Rutt BK. Biexponential longitudinal relaxation in white matter: characterization and impact on T1 mapping with IR-FSE and MP2RAGE. *Magn Reson Med.* 2016;75:2265–2277.
55. Bouhrara M, Spencer RG. Rapid simultaneous high-resolution mapping of myelin water fraction and relaxation times in human brain using BMC-mcDESPOT. *NeuroImage.* 2017;147:800–811.
56. Voigt T, Homann H, Katscher U, Doessel O. Patient-individual local SAR determination: In vivo measurements and numerical validation. *Magn Reson Med.* 2012;68:1117–1126.
57. Gabriel C. *Compilation of the dielectric properties of body tissues at RF and microwave frequencies.* London, UK: Department of Physics, King's College of London; 1996.

58. Kellner E, Dhital B, Kiselev VG, Reiser M. Gibbs-ringing artifact removal based on local subvoxel-shifts. *Magn Reson Med.* 2016;76:1574–1581.
59. Mandija S, Sbrizzi A, Katscher U, Luijten PR, van den Berg C. Error analysis of helmholtz-based MR-electrical properties tomography. *Magn Reson Med.* 2018;80:90–100.
60. Taylor JR. *An Introduction to Error Analysis: The Study of Uncertainties in Physical Measurements.* Sausalito, CA: University Science Books; 1997.
61. Gudbjartsson H, Patz S. The Rician distribution of noisy MRI data. *Magn Reson Med.* 1995;34:910–914.
62. Kellman P, McVeigh ER. Image reconstruction in SNR units: a general method for SNR measurement. *Magn Reson Med.* 2005;54:1439–1447.
63. Katscher U, Stehning C, Tha KK. The impact of CSF pulsation on reconstructed brain conductivity. In Proceedings of the 26th Annual Meeting of ISMRM, Paris, France, 2018. p. 0546.
64. Zhong K, Leupold J, von Elverfeldt D, Speck O. The molecular basis for gray and white matter contrast in phase imaging. *NeuroImage.* 2008;40:1561–1566.
65. Miller KL. Asymmetries of the balanced SSFP profile. Part I: theory and observation. *Magn Reson Med.* 2010;63:385–395.
66. Katscher U, Börner P, Leussler C, Van denBrink JS. Transmit SENSE. *Magn Reson Med.* 2003;49:144–150.
67. Cukur T. Accelerated phase-cycled SSFP imaging with compressed sensing. *IEEE Trans Med Imaging.* 2015;34:107–115.
68. Lee SK, Bulumulla S, Hancu I. Theoretical investigation of random noise-limited signal-to-noise ratio in MR-Based electrical properties tomography. *IEEE Trans Med Imaging.* 2015;34:2220–2232.
69. Wood T, Combes A, Shaihan M. Elliptical magnetization transfer: calculating MT parameters from the bSSFP signal ellipse. In Proceedings of the 26th Annual Meeting of ISMRM, Paris, France, 2018. p. 0789.
70. Li C, Gore JC, Davatzikos C. Multiplicative intrinsic component optimization (MICO) for MRI bias field estimation and tissue segmentation. *Magn Reson Imaging.* 2014;32:913–923.

SUPPORTING INFORMATION

Additional supporting information may be found online in the Supporting Information section at the end of the article.

FIGURE S1 Accuracy of transceive phase estimation for bSSFP (first column) and PLANET (second column): results from simulation I and III. Simulation I: $e_{\phi^{\pm}}$ as a function of FA and TR for a single-component voxel at $\Delta f_0 = 0$ Hz (first row) and at $\Delta f_0 = 30$ Hz (second row). WM: $T_1 = 832$ ms, $T_2 = 80$ ms and $\phi^{\pm} = -\pi/3$ rad. Simulation III: $e_{\phi^{\pm}}$ as a function of FA and TR for a 2-component voxel (third row). First component: WM, input $\Delta f_{0,1} = 0$ Hz, $\phi_{1,1}^{\pm} = -\pi/3$ rad, $T_{1,1} = 832$ ms, $T_{2,1} = 80$ ms and $w_1 = 0.88$. Second component: myelin, input $\Delta f_{0,2} = 35$ Hz (CS = 20 Hz), $\phi_{2,2}^{\pm} = -\pi/3$ rad, $T_{1,2} = 400$ ms, $T_{2,2} = 20$ ms, $w_2 = 0.12$

FIGURE S2 Precision of transceive phase estimation for bSSFP (left) and PLANET (right): results from simulation I and III. Image SNR (as calculated in Equation 6) and the transceive phase uncertainty $\zeta_{\phi^{\pm}}$ (as calculated in Equation 4) are shown as a function of FA and TR. Simulation I: image SNR

and $\zeta_{\phi^{\pm}}$ for a single-component voxel at $\Delta f_0 = 0$ Hz (first row) and at $\Delta f_0 = 30$ Hz (second row). Simulation III: image SNR and $\zeta_{\phi^{\pm}}$ for a 2-component voxel at $\Delta f_{0,1} = 0$ Hz (third row)

FIGURE S3 Effect of the number of RF dummy pulses. (A) Complex phase-cycled bSSFP signal sampled at different numbers of RF dummy pulses (# RF dummy pulses: 250, 500, 750, 1250 and 2500). The phase-cycled signal was simulated for one voxel with the following parameters (Simulation V): $T_1 = 3858$ ms and $T_2 = 500$ ms (representing maximum values found in CSF from T_1 and T_2 maps obtained with PLANET); $\Delta f_0 = 15$ Hz and $\phi^{\pm} = -\pi/3$ rad. MR parameters settings were: FA = 25° , TR = 4.6 ms, TR = TE/2 and $\Delta\theta_n = 2n\pi/8 - \pi$ with $n = \{0,1,2,\dots,7\}$. The ‘*’ represents the phase-cycled data corresponding to a certain $\Delta\theta_n$. The ‘*’ encircled in a red circle represents the bSSFP data with $\Delta\theta_n = -\pi$ rad, i.e. the standard bSSFP. Solid lines indicate the fitted ellipses during PLANET post-processing. (B) Transceive phase error $\Delta\phi^{\pm}$ as a function of RF dummy pulses. The transceive phase error was calculated as the difference between the transceive phase estimated at a certain dummy pulse ($\phi_{\#RF}^{\pm}$) and the true transceive phase ($\phi_{\text{true}}^{\pm} = -\pi/3$ rad) for both bSSFP and PLANET

FIGURE S4 Effect of eddy-current-induced phase accumulation on the phantom transceive phase and conductivity for bSSFP (left) and PLANET (right). The effect on the transceive phase is shown with a difference map calculated as $\Delta\phi_{\text{bSSFP/PLANET}}^{\pm} = \phi_{(+/-)\text{bSSFP/PLANET}}^{\pm} - \phi_{SE}^{\pm}$ where the subscripts “(+/-)” refer to the single acquisition with either positive “(+)” or negative “(-)” gradient polarity G. A linear phase gradient with reverse direction is visible along the readout direction (anterior-posterior in this case) according to the gradient polarity considered. Results are displayed for Experiment I and can be compared with maps shown in Figures 5 and 7

FIGURE S5 Phantom transceive phase and conductivity for all methods from Experiment III, where volume-based shimming was performed. For PLANET, the effect of using different N phase step increments on the transceive phase and conductivity is shown. Transceive phase maps for: (A) bSSFP; (B) PLANET with $N = 6$ (scan time: 04:04 min); (C) PLANET with $N = 8$ (scan time: 05:20 min); (D) PLANET with $N = 10$ (scan time: 06:47 min); (E) SE (reference method), after unwrapping. Conductivity maps reconstructed from transceive phase maps estimated with (F) bSSFP; (G) PLANET with $N = 6$; (H) PLANET with $N = 8$; (I) PLANET with $N = 10$; (J) SE. Conductivity (mean \pm SD) values are reported above the maps. Mean and SD were calculated within the circular ROI (shown in magenta color in (J)) in the central slice of the phantom. (K) Transceive phase profiles of bSSFP, PLANET (with the 3 different N) and SE, calculated on the central horizontal line (dashed line in (E)). (L) Boxplot of conductivity values, evaluated in the circular ROI. The true conductivity value, as measured by the dielectric probe, is shown with a black dashed line

FIGURE S6 Effect of eddy current-induced phase accumulation on the transceive phase and the conductivity for bSSFP (left) and PLANET (right). Results are displayed for volunteer 1 and can be compared with maps shown in Figures 8 and 9. The effect on the transceive phase is shown with a difference map calculated as $\Delta\phi_{bSSFP/PLANET}^{\pm} = \phi_{(+/-)bSSFP/PLANET}^{\pm} - \phi_{SE}^{\pm}$ where the subscripts “(+/-)” refer to the single acquisition with either positive “(+)” or negative “(-)” gradient polarity G . Reversed linear phase gradients occur along the readout direction (anterior-posterior in this case) according to the gradient polarity considered; these gradients, however, were not perfectly “mirrored” thus a residual eddy-current-induced phase remains visible when the two phase images are averaged to obtain the transceive phase (e.g., on the left side of frontal lobe, Figure 9)

FIGURE S7 In vivo brain results for volunteer 2 (A-H) and 3 (I-P), obtained with bSSFP (first column), PLANET (second column) and SE (reference, third column) methods. Isotropic voxel size: 2.5 mm. Transceive phase maps (ϕ^{\pm}) obtained from (A,I) bSSFP; (B,J) PLANET and (C,K) SE after unwrapping. (D,L). Banding-free magnitude image obtained with PLANET method. Conductivity maps based on (E,M) bSSFP; (F,N) PLANET and (G,O) SE, reconstructed from transceive phase maps shown in (A-C, I-K) respectively. (H,P) Δf_0 map

How to cite this article: Gavazzi S, Shcherbakova Y, Bartels LW, et al. Transceive phase mapping using the PLANET method and its application for conductivity mapping in the brain. *Magn Reson Med*. 2020;83: 590–607. <https://doi.org/10.1002/mrm.27958>

APPENDIX

THE BSSFP SIGNAL

The complex bSSFP signal inside a voxel in the steady state regime is expressed as⁴³

$$I_0 = KM \cdot e^{-\frac{TE}{T_2}} \cdot \frac{1 - E_2 e^{-i(\theta_0 + \pi)}}{1 - b \cos(\theta_0 + \pi)} \cdot e^{i\Omega}, \quad \text{for } E_{1,2} = e^{-\frac{TR}{T_{1,2}}} \quad (\text{A1})$$

where K is a proportionality constant which includes the magnitude of the receive coil sensitivity. Definition of M and b is as follows:

$$M = \frac{M_0 (1 - E_1) \sin(FA)}{1 - E_1 \cos(FA) - E_2^2 (E_1 - \cos(FA))} \quad (\text{A2})$$

$$b = \frac{E_2 (1 - E_1) (1 + \cos(FA))}{1 - E_1 \cos(FA) - E_2^2 (E_1 - \cos(FA))} \quad (\text{A3})$$

which both depend on TR , relaxation times T_1 and T_2 through $E_{1,2} = e^{-\frac{TR}{T_{1,2}}}$ and FA . The phase components θ_0 and Ω depend on: chemical shift (CS, in Hz), off-resonance caused by B_0 field variations (Δf_0 , in Hz), transceive phase (ϕ^{\pm}), eddy currents due to ramping of readout gradient G (ϕ_{eddy}), the gradient polarity ($sign(G)$) and B_0 drift (ϕ_{drift}):

$$\theta_0 = 2\pi (CS + \Delta f_0) TR \quad (\text{A4})$$

$$\Omega = 2\pi (CS + \Delta f_0) TE + \phi^{\pm} + \phi_{drift} + sign(G) \cdot \phi_{eddy} \quad (\text{A5})$$